# AB INITIO MODELING OF HYDROGEN PIPE DIFFUSION IN PALLADIUM

BY

EMILY SCHIAVONE

DISSERTATION

Submitted in partial fulfillment of the requirements
for the degree of Doctor of Philosophy in Materials Science and Engineering
in the Graduate College of the
University of Illinois at Urbana-Champaign, 2017

Urbana, Illinois

Doctoral Committee:

Associate Professor Dallas R. Trinkle, Chair and Director of Research
Professor Pascal Bellon
Professor Brent Heuser
Assistant Professor Andre Schleife

# ABSTRACT

A hydrogen economy will require metals for separation, transport and/or storage. Therefore, we need to better understand the behavior of hydrogen in metals. Hydrogen in palladium is a model system, for which there exists an abundance of experimental data. Specifically, quasielastic neutron scattering (QENS) experiments, for the first time, directly measured hydrogen pipe diffusion. The diffusivities and energy barriers from ab initio simulations support these findings, but open questions remain, the most concerning of which pertains to the unusual jump distances reported from fitting the experimental data. Instead of comparing diffusivities and energy barriers from simulation with the parameters extracted from fits to the experimental data, we calculate the spherically-averaged incoherent scattering function to directly compare with experimental data. We find that the experimental fitting procedure introduces errors in the extracted diffusivities and jump distances. We also calculate the intermediate scattering function to compare our simulation results with a wider range of experimental data. From direct comparison of the intermediate scattering function, we find disagreement at small times, which is likely due to the contributions from the vibrational motion of the diffusing hydrogen atom, the host palladium atoms and resonate vibrations. This computational approach allows for validation against experiment, along with a more detailed understanding of the QENS results.

*To Dad, Mom, Rose, Will and Mary.*

# ACKNOWLEDGMENTS

First, I would like to thank my advisor Dallas Trinkle for introducing me to the project and for his advice and support throughout the course of this work.

I would also like to thank my thesis committee members: Professor Pascal Bellon, Professor Brent Heuser and Professor Andre Schleife for their support and guidance.

I would like to thank past and current graduate students in the Trinkle group: Henry Wu, Joseph Yasi, Maryam Ghazisaeidi, Pinchao Zhang, Zebo Li, Ah-Young Song, Abhinav Jain, Ravi Agarwal, Anne Marie Tan, Hyojung Kim, and Yang Dan. I also want to thank past and current postdoctoral researchers: Venkateswara Rao Manga, Thomas Garnier, Bora Lee, Mike Fellinger, and Thomas Schuler. I want to thank Joseph Serio from the Department of Nuclear, Plasma, and Radiological Engineering for his help understanding the experimental data and analysis. I would also like to thank the professors in addition to my advisor for whom I was a teaching assistant, Professor Robert Maass and Professor Jessica Krogstad, as well as Professor John Abelson for his friendship and career advice.

I am grateful for the friendships that carried with me through my time in graduate school: Liza Dickinson, Kimberly Foley, Jessica Heller, Christine Menzenberger, Katie Sebens, Jenna Shumaker, Lauren Clifford, and Kevin Hill as well as the friendship and support I found in the Champaign community, especially the Illini women's water polo club and the Champaign-Urbana poetry group.

I am indebted to Carthage water polo team and to the mathematics and physics faculty at Carthage College for helping me figure out what I wanted to do and helping me get here: Douglas Arion, Temple Burling, Charolette Chell, Kevin Crosby, Julie Dahlstrom, Jean Quashnock, Brian Schwartz, Mark Snavely, Aaron Trautwein, and Erlan Wheeler.

This research was funded by NSF under Grant No. DMR-1207102. This work used the Extreme Science and Engineering Discovery Environment (XSEDE),[1] which is supported by National Science Foundation grant number ACI-1053575 at the Texas Advanced Computing Center; and the Taub cluster at Univ. Illinois, Urbana-Champaign.

# TABLE OF CONTENTS

# LIST OF FIGURES

# LIST OF ABBREVIATIONS

| | |
|---|---|
| DFT | Density-Functional Theory |
| KMC | Kinetic Monte Carlo |
| QENS | Quasielastic Neutron Scattering |
| fcc | face-centered cubic |
| T | Tetrahedral |
| O | Octahedral |
| TEM | Transmission Electron Microscopy |
| CE | Chudley-Elliot |

# LIST OF SYMBOLS

| | |
|---|---|
| $a$ | Equilibrium lattice parameter |
| $E_O$ | Octahedral site energy |
| $E_T$ | Tetrahedral site energy |
| $E_{OT}$ | Octahedral site to tetrahedral site energy barrier |
| $E_{TO}$ | Tetrahedral site to octahedral site energy barrier |
| $D$ | Diffusion coefficient |
| $\varepsilon_T$ | Tetrahedral site strain |
| $\varepsilon_O$ | Octrahedral site strain |
| $\beta$ | Thermodynamic beta |
| $\hbar$ | Planck constant |
| $\nu_{mn}$ | Jump rate from site $m$ to $n$ |
| $\mathbf{s}_{mn}$ | Jump vector from site $m$ to $n$ |
| $s$ | Jump distance |
| $\tau$ | Residence Time |
| $\omega$ | Frequency |
| $\mathbf{k}_i$ | Incoming wavevector |
| $\mathbf{k}_f$ | Scattered wavevector |
| $\mathbf{Q}$ | Scattering wavevector $\left(\mathbf{k}_f - \mathbf{k}_i\right)$ |
| $Q$ | Scattering wavenumber |
| $\rho$ | Site probability |

| | |
|---|---|
| $\Lambda$ | Jump matrix |
| $\tilde{\Lambda}$ | Hermitian jump matrix |
| $\tilde{\lambda}_i$ | Eigenvalue of Hermitian jump matrix (width of Lorentzian term) |
| $\tilde{e}$ | Eigenvector of Hermitian jump matrix |
| $w_i(\mathbf{Q})$ | Weights of Lorentzian terms |
| $W(Q;\lambda)$ | Density of rates |
| $S_{\text{inc}}(\mathbf{Q},\omega)$ | Incoherent scattering function |
| $S_{\text{inc}}(Q,\omega)$ | Spherically averaged incoherent scattering function |
| $I_s(\mathbf{Q},t)$ | Self-part of the intermediate scattering function |
| $I_s^d(\mathbf{Q},t)$ | Self-part of the intermediate scattering function due to diffusion |
| $I_s^v(\mathbf{Q},t)$ | Self-part of the intermediate scattering function due to vibrations |
| $\chi^2$ | Least-squares fit |
| $\Gamma$ | Lorentzian width |
| $\tau_{\text{KWW}}$ | KWW decay constant |
| $\beta$ | Shape parameter |

# CHAPTER 1

# INTRODUCTION

This work is a fundamental study of the behavior of hydrogen near a dislocation in a metal. The investigation of hydrogen in metals contributes to the understanding of hydrogen embrittlement and is a necessary step towards the realization of the use of hydrogen as an energy storage medium. We will focus on hydrogen in palladium as a model hydrogen-metal system. Specifically, we are interested in determining the effect of the strain field due to a dislocation on hydrogen diffusion in palladium. Quasielastic neutron scattering is a powerful experimental technique that probes hydrogen diffusion. Our work aims to develop the understanding of incoherent quasielastic neutron scattering data for diffusion in an anisotropic system.

## 1.1 Hydrogen in metals

### 1.1.1 Hydrogen embrittlement

Knowledge of the behavior of hydrogen in metals is crucial for understanding hydrogen-related failure in steels, aluminum alloys, and titanium[2–7]. Hydrogen embrittlement can lead to catastrophic failure of metals [8]. In March of 2013, the 32 of the 96 San Francisco Oakland Bay bridge anchor rods cracked about a week after tightening[9]. Brahimi *et al.* analyzed the failed anchor rods and found evidence of brittle fracture: intergranular cracking and a lack of elongation. This evidence combined with the delayed fracture of the anchor rods pointed to hydrogen embrittlement as the failure mechanism of the anchor rods, likely due to exposure to water between the time of their installation in 2008 and the time of tightening five years later. Hydrogen can lead to

blistering, cracking due to hydride formation, hydrogen attack, decreases in fatigue resistance, and internal crack formation[10].

With increasing hydrogen concentrations, hydrogen will form hydrides in many metals including zicronium, titanium, nickel, niobium, and vanadium[11]. The presence of a single hydrogen atom distorts the metal lattice by about 2.8 $Å^3$ per hydrogen atom[12]. In dilute concentrations, the metal hydrogen systems exhibits a disordered phase. As the concentration of hydrogen increases an ordered phase the system precipitates out an ordered metal hydride. The metal hydride expands the metal lattice by about 0.3–0.7 $Å^3$ per hydrogen atom at these higher hydrogen concentrations, which induces stresses[8, 12]. Nasako *et al.* studied the stress on a reaction vessel filled with metal alloy particles due to hydrogen absorption/desorption cycling[13]. The stress from the expanding metal alloy increased linearly with the number of cycles. The cycling also led to the powderization of some of the particles, which fell to the bottom of the reaction vessel creating an uneven distribution of stress and plastic deformation of the bottom of the vessel. The stress continued to increase even after the vessel began to plastically deform. Furthermore, metal hydrides are brittle and facilitate crack propagation.

Hydrogen absorbed by molten metal precipitates out at voids and interfaces as temperature decreases, which prevents blunting of crack tips and promotes their extension into the metal[8]. This hydrogen induced cracking is observed as snowflakes and fisheyes. A snowflake refers to the the texture of the surface of a metal after tensile failure, which consists of small flat, reflective surfaces. The formation of snowflakes is due to a localized decrease in ductility[2]. The area of local hydrogen embrittlement extends away from the fracture surface, which is a cross section of a spherical region of hydrogen embrittlement. Fisheyes are areas of local hydrogen embrittlement surrounding a hydrogen gas filled void. Khinskii and Krylov found that the number and size of fisheyes that develop in steel depend on the amount of hydrogen content present and the amount of plastic deformation[14]. Removing hydrogen from the steel eliminates the fisheyes.

Hydrogen attack refers to the irreversible formation of methane bubbles due to exposure of steel to high pressure hydrogen at high temperatures[15]. The growth and merging of the methane

bubbles causes a sudden reduction in ductility and strength of the material. Thygeson and Molstad investigated changes in volume, carbon content, microstructure, and ultimate strength due to hydrogen attack in steel[16]. These authors found that the ultimate strength elucidated three periods in the development of hydrogen attack: an induction period, a maximum attack rate period, and a low attack rate period. The ultimate strength was linearly related to residual carbon content, and the change in volume of the steel correlated linearly with the loss of carbon content. Micrographs of the steel samples showed that the hydrogen attack originated inside the metal rather than at the surface. Ransick and Shewmon observed that deforming steel enhanced the nucleation of methane bubbles and altered the formation of fissures[17]. In regions of high tension or compression, fissures formed along grain boundaries in contrast to the fissures primarily formed near inclusions in undeformed samples. Furthermore, Ransick and Shewmon postulated that the high density fissures in the deformed steel became interconnected, providing pathways for the methane gas to travel to the surface of the metal.

Heat treatments to eliminate hydrogen embrittlement may leave behind enough hydrogen to form blisters, where hydrogen precipitates induce pressure at interfaces[8]. Treischel identified hydrogen from the acid pickling process as the source of blistering between an enamel coating and sheet steel[18]. Ren *et al.* proposed a mechanism for hydrogen blister formation in that the hydrogen interstitials increased the equilibrium concentration of vacancies, stabilized vacancies clusters and formed hydrogen molecules in the hydrogen-vacancy clusters[19]. Hydrogen interstitials and vacancies migrate freely at room temperature to the hydrogen-vacancy cluster. Once the cluster reaches a critical size, cracks form along the edges of the cluster extending into the metal matrix.

There are several proposed mechanisms for hydrogen-related failure, and it is possible that multiple mechanisms contribute to deleterious changes in material properties[8, 20], several of which involve hydrogen-dislocation interactions[21]. Dislocations enhance both internal and external hydrogen embrittlement[7]. Dislocations increase the penetration depth of hydrogen in cases where the surface of a metal is exposed to hydrogen. Donovan exposed tensile tubes of iron, strained the tubes, and observed an increase of hydrogen in the regions of the tube that underwent plastic

deformation relative to the regions of the tube that underwent elastic deformation[22]. Donovan found a difference in trend of the hydrogen concentration as a function of penetration depth for cold worked tubes relative to the annealed tubes and attributed this difference to diffusion short circuits. Louthan *et al.* observed reduced hydrogen embrittlement in coated stainless steel exposed to a hydrogen pressure of 10,000 psi during short-time plastic deformation tests relative to uncoated stainless steel and stainless steel coated after the initial onset of plastic deformation[3]. The coating prevents hydrogen from entering the metal during the initial onset of plastic deformation, which is dominated by surface slip. After this initial phase, the surface hardens preventing additional surface slip and the associated enhanced hydrogen embrittlement. Kurkela and Latanision measured effective diffusivities of hydrogen in plastically deformed nickel that were five orders of magnitude higher than the diffusivity of hydrogen in unstrained nickel[23]. Dislocations also accelerate the diffusion of hydrogen already present in a metal matrix, delivering it to potential crack nucleation sites[7].

### 1.1.2 Metals as a part of a hydrogen economy

Understanding the behavior of hydrogen in metals is also necessary for considering metals for separation[24], transport[25], and storage[26, 27] of hydrogen as a part of a hydrogen economy. Hydrogen can be stored in a variety of ways, each with its own benefits and limitations[28]. Storing hydrogen in a high pressure tank is relatively cheap and an already established method, however this method is dangerous and not practical for mobile applications. Cooling hydrogen down to temperatures where it transforms into a liquid or a solid allows for a denser storage of hydrogen compared to high pressure tanks. It is energetically expensive to store hydrogen as a liquid or as a solid, and hydrogen stored in this manner can be lost to evaporation. The evaporation issue can be minimized by storing large amounts of hydrogen and reducing the ratio of the surface area to volume. Metal hydrides offer dense hydrogen storage near room temperature. In some metals, the high solubility of hydrogen can lead to hydrogen concentrations of 100 at.% and the light hydrogen atom diffuses[29]. Hydrogen also diffuses faster than other, heavier elements. Dislocations

increase hydrogen solubility and reduce diffusion energy barriers, both of which are attractive modifications for the commercialization of metal for hydrogen storage[30–32]. Flanagan et al. studied the solubility in cold rolled palladium and cold worked chips of palladium and found similar solubility enhancements for both hydrogen and deuterium relative to their solubilities in well annealed palladium[33]. The interaction of hydrogen atoms with dislocations in metals is complex, scientifically relevant, and deserves investigation.

### 1.1.3 Hydrogen in palladium

Hydrogen in palladium is an ideal system to study due to the abundance of experimental data with which to compare. Palladium is a face-centered cubic (fcc) crystal with a lattice parameter of 3.872Å at 4.2K[34]. Palladium alloy membranes are currently used in industry to separate hydrogen from other gasses[35]. This use stems from the catalytic property of the palladium surface that causes spontaneous dissociation of adsorbed hydrogen molecules, which then diffuse into the bulk[36, 37]. Fig. 1.1 shows the two stable interstitial sites for hydrogen in palladium: an octahedral (O) site and a tetrahedral (T) site. Each O site is connected to eight nearest neighbor T sites, and each T site is connected to four nearest neighbor O sites. For each palladium atom in the fcc crystal, There are two symmetrically unique T sites and one O site. All of the O sites are symmetrically equivalent and make up a Bravais lattice. The ground state is the O site, and it is well known that hydrogen diffuses through bulk palladium via an O-T-O transition pathway[38].

With increasing hydrogen concentrations, the palladium-hydrogen system begins to precipitate out a hydride phase, often termed the $\beta$- or $\alpha'$-phase[39, 40]. The $\beta$-phase indicates an ordered phase in which the hydrogen atoms change the planar spacing of the lattice creating planes that are completely filled or completely void of hydrogen atoms[27], in contrast to the $\alpha$-phase of palladium hydride which corresponds to a random distribution of hydrogen as interstitials in the fcc palladium lattice. Overall, the formation of the $\beta$-phase of palladium hydride expands the lattice. The nonuniform growth of this phase creates strains within the lattice that lead to distortion, dislocation multiplication, and hardening[41].

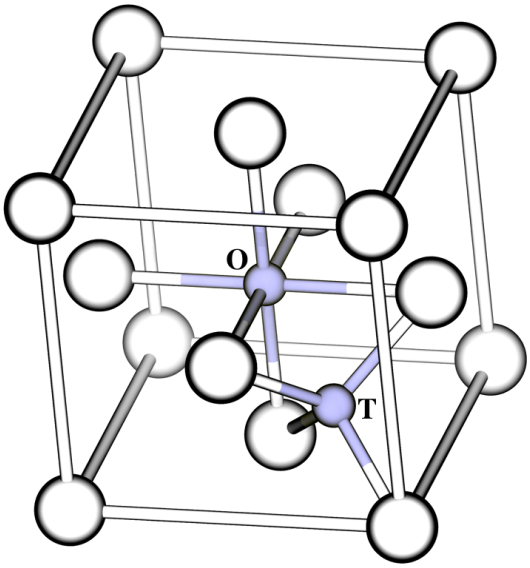


Figure 1.1: Bulk palladium interstitials sites. The palladium atoms are shown in white, and the interstitials sites are purple. The octahedral site (O) has six palladium neighbors, and the tetrahedral site (T) is surrounded by four palladium atoms.

Sites with energies lower than the site energy of an octahedral site in bulk near a dislocation lead to trapping of hydrogen[42] thus elevated hydrogen concentrations[43] and the formation of nanoscale hydrides[44, 45]. The formation of these hydrides could prohibit pipe diffusion along the dislocation. Heller and Wipf experimentally measured diffusivities that decreased with increasing hydrogen concentrations in vanadium[46]. An atomistic study of vanadium hydrides predicted slower diffusion near a dislocation than in bulk[47]. However, there is indirectly measured evidence of pipe diffusion of hydrogen in palladium[48].

## 1.2 Pipe diffusion

Accelerated diffusion of point defects along a dislocation, pipe diffusion, is often used to explain enhanced diffusion in deformed samples but is difficult to measure experimentally and to model[49–52]. Soon after Aust and Chalmers[53] proposed that grain boundaries consisted of an array of dislocations, Hart developed a simple model to predict the diffusvity enhancement due to randomly orientated dislocations in a composite formed by bulk and dislocation regions[50].

Turnbull and Hoffman suggested pipe diffusion to explain accelerated self-diffusion of silver along grain boundaries[49, 54]. Love and Shewmon observed a linear relationship between the diffusivity of silver in twist boundaries and the misorientation angle, corresponding to the density of dislocations[55]. The self-diffusivity of silver in a twist boundary was at least a factor of ten times smaller than the diffusivity measured by Turnbull and Hoffman. Love and Shewmon attributed this difference to the fact that the twist boundary is composed of screw dislocations rather than the edge dislocations in the tilt boundary studied by Turnbull and Hoffman. Love developed a model that takes into account the screw or edge character of the dislocations that make up the grain boundary[51]. Initial evidence for dislocation pipe diffusion was restricted to experimental observations of accelerated diffusion along grain boundaries, arrays of dislocations with varying separations[49, 55], and then tracer diffusion along arrays of widely separated dislocations[56]. Wuttig and Birnbaum activated a single slip system by bending single crystal bars of nickel, estimated dislocation density by counting etch pits, and studied the diffusion of tracer nickel atoms along the edge dislocations[56]. Later, Volin and Balluffi observed accelerated octahedral void shrinkage for voids connected to dislocations compared to voids in bulk aluminum using transmission electron microscopy (TEM)[57], and a model was developed to quantitatively estimate the diffusion rate from the void shrinkage rate, which was used to estimate the diffusion barrier for vacancies in bulk aluminum[58] and subsequently estimate the reduced diffusion barrier of vacancies near a dislocation in aluminum[59]. Tang *et al.* used TEM to study dislocation dipole annihilation in undoped and MgO-doped sapphire and estimated pipe diffusion coefficients assuming that the oxygen and aluminum point defects travelled along the dislocation to create dislocation loops[60]. More recently, Legros *et al.* used TEM to measure an accelerated dissolution rate of silicon precipitates connected by a dislocation in an aluminum thin film and extracted a pipe diffusion energy barrier[61]. A computational study by Zhang and Lu[62] of this same system supported these experimental findings. However, dislocations do not always lead to faster diffusion; one computational study used an embedded atom model potential and found reduced hydrogen diffusion along both screw and edge dislocations in iron due to high diffusion barriers[63].

In the study by Zhang and Lu, the authors predicted that the stacking fault between separated partial dislocations would contribute to pipe diffusion. Two early experiments claimed that faster diffusion in the stacking fault of separated partial dislocations may contribute to pipe diffusion[56, 64]. Baker *et al.* [64] extended the work by Wuttig and Birnbaum[56], which measured the tracer flux in a plastically deformed nickel wafer, to vacancy diffusion in nickel cobalt alloys. A 40% nickel and 60% cobalt alloy has a lower stacking fault energy than pure nickel, leading to larger separations between partial dislocation cores[64]. Baker *et al.* analyzed their data for diffusion in nickel cobalt using an elliptical cross section for the fast diffusion pathways and found that the effective radius determined by the separation of the partial dislocations agrees with the radius extracted from the data. However, Balluffi dismissed this idea, arguing that the stacking fault neighbor distances were similar to bulk and could not account for the observed accelerated diffusion[52], making an analogy with diffusion near a coherent twin boundary, which does not exhibit strongly anisotropic diffusion[65]. Two computational studies, in addition to the study on silicon precipitates in aluminum, indicated that the stacking fault between the partial dislocation cores contributes to accelerated diffusion[66, 67]. Fast diffusion along a stacking fault is still suggested to explain results in recent experiments[68].

Despite the established history of pipe diffusion as a proposed mechanism for accelerated diffusion in deformed materials[49–51, 59, 61, 69, 70], direct quantitative evidence of pipe diffusion is limited[71]. Previous studies of hydrogen near a palladium dislocation found the formation of hydrides in the dislocation core[45], which could block pipe diffusion. Von Pezold et al used an EAM potential, which they validated by *ab initio* simulations, along with a lattice gas Hamiltonian, with which they could switch the hydrogen-hydrogen interaction on and off, to study the interaction of hydrogen with dislocations in nickel[72]. These authors found that including hydrogen-hydrogen interactions reduced the concentration of hydrogen required to form hydrides near the dislocation core. Heuser *et al.* directly measured increased diffusivity and an energy barrier for hydrogen pipe diffusion in deformed palladium with quasielastic neutron scattering (QENS)[71]. Spectra of the incoherent scattering function $S_{\text{inc}}(Q,\omega)$ as a function of frequency $\omega$ from QENS exper-

iments are fit with a single Lorentzian, or sometimes a sum of two or more Lorentzians, for a given magnitude of the wavevector $Q$. The Lorentzian widths as a function of $Q$ can be fit with a Chudley-Elliott (CE) model[73] to extract jump distances and mean residence times, which yield diffusivities. Using this fitting approach, Heuser *et al.* found diffusion barriers lower than those predicted by density functional theory (DFT) calculations. In addition, the jump distances were much larger than bulk jump distances and nonmonotonic as a function of temperature. Information about diffusion mechanisms in solids and liquids can be extracted from QENS data[74], which is a promising technique for measuring pipe diffusion.

## 1.3 Quasielastic neutron scattering

Quasielastic neutron scattering experiments probe atomic scale diffusion[75]. Commonly, neutron scattering experiments measure intensity at deflection angles of outgoing neutrons and use Bragg peaks to determine crystal structure[76]. In addition to measuring scattering angle, QENS experiments measure the energy gain or loss of the scattered neutrons, which gives insight into the dynamics of the system. The intensity measured from a QENS experiment gives the double differential cross section

$$\frac{\partial^2\sigma}{\partial\omega\partial\Omega} = \frac{k_f}{k_i}\left(\frac{\sigma_{\text{coh}}}{4\pi}S_{\text{coh}}(\mathbf{Q},\omega) + \frac{\sigma_{\text{inc}}}{4\pi}S_{\text{inc}}(\mathbf{Q},\omega)\right), \tag{1.1}$$

which is composed of the coherent scattering function $S_{\text{coh}}(\mathbf{Q},\omega)$ and the incoherent scattering function $S_{\text{inc}}(\mathbf{Q},\omega)$ whose contributions are proportional to the coherent and incoherent scattering cross sections $\sigma_{\text{coh}}$ and $\sigma_{\text{inc}}$ and where $k_i$ and $k_f$ are the wave numbers of the incoming and scattered neutrons[75]. The scattering wavevector $\mathbf{Q} = \mathbf{k}_f - \mathbf{k}_i$ and $\omega$ is the frequency such that the energy transfer between the incident neutron and the diffusing atoms is $\hbar\omega$. The coherent scattering function

$$S_{\text{coh}}(\mathbf{Q},\omega) = \frac{1}{2\pi\hbar}\int_{-\infty}^{\infty}\int_{-\infty}^{\infty} e^{i(\mathbf{Q}\cdot\mathbf{r}-\omega t)}G(\mathbf{r},t)d\mathbf{r}dt \tag{1.2}$$

is the temporal and spatial Fourier transforms of the correlation function $G(\mathbf{r}, t)$[77]. Assuming that all the diffusing particles are identical, the classical $G(\mathbf{r}, t)$ or the probability of finding any particle at the position $\mathbf{r}$ at time $t$ given a particle at the origin at $t = 0$, is

$$G(\mathbf{r}, t) = \sum_i \langle \delta \left( r - (r_i(t) - r_0(0)) \right) \rangle \tag{1.3}$$

where $\delta$ is the Kronecker delta[78]. The angular brackets denote an ensemble average. Similarly, the incoherent scattering function

$$S_{\text{inc}}(\mathbf{Q}, \omega) = \frac{1}{2\pi\hbar} \int_{-\infty}^{\infty} \int_{-\infty}^{\infty} e^{i(\mathbf{Q}\cdot\mathbf{r} - \omega t)} G_s(\mathbf{r}, t) d\mathbf{r} dt \tag{1.4}$$

is the temporal and spatial Fourier transforms of the self correlation function $G_s(\mathbf{r}, t)$, or given a particle at the origin at $t = 0$, the probability of finding the same particle at the position $\mathbf{r}$ at time $t$, i.e.

$$G_s(\mathbf{r}, t) = \langle \delta \left( r - (r_0(t) - r_0(0)) \right) \rangle. \tag{1.5}$$

Coherent QENS is characteristic of collective diffusion, while incoherent QENS is related to the diffusion of a single particle.

The use of incoherent QENS is limited to only a few elements and is particularly effective for studying the diffusion of hydrogen. This limitation is due to the fact that many elements have larger coherent scattering cross sections than incoherent scattering cross sections[79]. The most elementary atom, hydrogen, is central to many physically important systems including water[80], methane[81, 82], and metal hydrides. The double differential cross section of hydrogen is dominated by the incoherent term, which disrupts the analysis of the coherent scattering and determining structure information of systems containing hydrogen but allows for the study of diffusion through the analysis of the incoherent scattering[79].

### 1.3.1 Chudley-Elliott model

Many studies have contributed to the analysis and understanding of neutron scattering data[73, 77, 80, 83–86]. Van Hove introduced the relationship between neutron scattering and correlation functions and predicted that diffusion in liquids would behave similarly to a gas[77]. Vineyard predicted that the incoherent scattering function could be fit with Lorentizans whose widths, for small $Q$, were related to the diffusivity $D$ by $DQ^2$[83]. Early QENS experiments on liquid water[80, 84, 85] and lead[87, 88] attempted to verify Vineyard's analytical model[80, 84, 85, 87] and transformed the double differential cross section to experimentally determine a correlation function for the first time[88]. Pelah *et al.* found that Vineyard's model did not capture the behavior of the widths of Lorentzians fit to the scattering data[87]. The experiments by Hughes *et al.* showed that the atomic motions in water were more similar to atomic motions in ice than in vapor[85]. Chudley and Elliott developed models that predict incoherent scattering in liquids, cubic lattices, and close-packed lattices[73]. The widths of Lorentzians for a given isotropic arrangement of sites are given by

$$\Gamma(Q) = \frac{\hbar}{n\tau} \sum_j \left(1 - \exp(iQs_j)\right), \tag{1.6}$$

where $n$ is the number of neighboring sites. Chudley and Elliott modeled a liquid as having short-range order in the form of a cage of nearest neighbor sites, similar to an isotropic crystal but no long-range order. Spherically integrating the widths in Eqn. (1.6) over $\mathbf{Q}$ yields the isotropic Chudley-Elliott model for the widths of Lorentzians from diffusion in liquids

$$\Gamma_{\mathrm{CE}}(Q) = \frac{\hbar}{\tau}\left(1 - \frac{\sin(Qs)}{Qs}\right), \tag{1.7}$$

where $\tau$ is the residence time and $s$ is the jump distance. Using the parameters from the CE model, the diffusivity is

$$D_{\mathrm{CE}} = \frac{s^2}{6\tau}. \tag{1.8}$$

The model developed by Chudley and Elliott for isotropic diffusion as well as generalized forms[78, 89, 90] of the model are widely used[91, 92]. Diffusion within a Bravais lattice can be approximated as isotropic diffusion[86]. Some defect diffusion networks in certain crystal structures make up Bravais lattices, such as octahedral sites in an fcc crystal. Analysis of QENS data for hydrogen diffusion in single crystal and polycrystalline fcc palladium has been established and validated[93]. Rowe *et al.* extended the model developed by Chudley and Elliott to study diffusion of hydrogen between the interstitial sites in vanadium, a body-centered cubic lattice, which do not form a Bravais lattice[89]. Richter and Spinger developed a two-state random walk model and a continuum model to investigate diffusion near trap sites[94]. The two-state random walk model describes the the experimental widths $\Gamma$ from diffusion of hydrogen in niobium with nitrogen trapping impurities up to $Q \approx 1\text{Å}^{-1}$ and the elastic continuum model describes the widths at large $Q$. Frenken *et al.* modeled the helium-atom scattering from self-diffusion in the lead (110) surface as diffusion in a rectangular lattice[95]. Funke *et al.* generalized the Chudley-Elliott model to include correlated forward and backward hops to investigate the motion of silver ions in a solid electrolyte[90]. Analyzing QENS data for more complex systems is difficult and can lead to seemingly different results depending on the model used to fit the data[96]. Developing an understanding of QENS data will allow for hydrogen to be used as a probe in a variety of systems.

### 1.3.2 Intermediate scattering function

In contrast to the incoherent scattering function measured by QENS experiments, neutron spin-echo experiments measure the normalized intermediate scattering function[97]. Spin-echo experiments cover a smaller (larger) energy (time) range than time-of-flight and backscattering experiments[98]. The (coherent) intermediate scattering function is the spatial Fourier transform of the pair correlation function, Eqn. (1.3),

$$I(\mathbf{Q}, t) = N^{-1} \sum_{i}^{N} \sum_{j}^{N} \langle \exp\left(i\mathbf{Q} \cdot (\mathbf{r}_j(t) - \mathbf{r}_i(t_0))\right) \rangle, \tag{1.9}$$

where $N$ is the number of atoms[78]. The self-part of the intermediate scattering function, analogous to the incoherent scattering function, consists of only the terms where $i = j$, equals one at $t = 0$, and decays to zero for long range diffusion. The self-part of the intermediate scattering function $I_s(\mathbf{Q}, t)$ is the product of the diffusional and vibrational contributions.

$$I_s(\mathbf{Q}, t) = I_s^v(\mathbf{Q}, t) \cdot I_s^d(\mathbf{Q}, t). \tag{1.10}$$

In general, the vibrational contribution can be neglected[74]. The data from QENS experiments can be converted into the intermediate scattering function via discrete Fourier transforms. Howells discrete Fourier transformed data from four different instruments to find that the intermediate scattering for the polymer polymethyl methacrylate cannot be described by a single decaying exponential (or a single Lorentzian in frequency space) for any temperature[96]. Howells combined the transformed data to show that the data from different instruments overlaps, even though the widths of the Lorentzians fit to the original data seemed to disagree.

### 1.3.3 Kohlraush-Williams-Watts model

The decay of the intermediate scattering function over time cannot always be described using a single decaying exponential. Williams and Watts proposed a model for the dielectric relaxation of polymers

$$\phi(t) = \exp\left(-\left(\frac{t}{\tau}\right)^{\beta}\right), \tag{1.11}$$

where the decay constant $\tau$ and shape parameter $\beta$ are fitting parameters[99]. Kohlrausch suggested this relaxation function as early as 1866 to describe the mechanical creep[100]. Williams and Watts mentioned that this function corresponds to a certain distribution of rates, but did not investigate the form of this distribution nor its significance. These authors stressed the importance of developing a theory to support the use of this model for a physical system, which is challenging.

The Kohlraush-Williams-Watts (KWW) model, called the stretched exponential function or

fractional exponential function, successfully describes the data from a variety of physical systems. Patterson recommended the KWW model to describe optical scattering data from the motion of polymer molecules due to its success in fitting the data and its established use[101]. Jones *et al.* found success with the KWW model for predicting the position and shape of the loss peak from nuclear magnetic resonance measurements of bulk polycarbonate, and the KWW model produced physically reasonable parameters[102]. Chamberlin *et al.* applied a magnetic field to a spin-glass, which is a disordered magnet, removed the magnetic field, and measured the relaxations of spins over time[103]. The KWW model characterized the decay of these relaxations over time. Le Grand strained polymers, unloaded them measuring the length and birefringence over time, and applied the KWW model to the mechanical relaxation of the polymers[104]. The KWW model is also used to fit the conductivity modulus in glassy fast ion conductors [105]. Svare *et al.* studied the distribution of relaxation times associated with the fits of the KWW to the conductivity of lithium ions. Overall, the KWW model is useful for systems that deviate from simple exponential decay.

## 1.4 Research scope

This work touches on three major topic areas: hydrogen in metals, pipe diffusion, and quasielastic neutron scattering. In the following chapters, we will use computational tools to investigate hydrogen pipe diffusion in palladium. We choose to study hydrogen in palladium, but the qualitative findings from this system may also be relevant for hydrogen in other fcc metals. Chapter 2 discusses the diffusion network for hydrogen diffusion in palladium in the bulk and near an edge dislocation. From the network near a dislocation, we propose a mechanism that allows the diffusing hydrogen atoms to circumvent neighboring hydrogen atoms, which would potentially inhibit its motion. We also compute diffusivity via kinetic Monte Carlo simulations, find evidence of pipe diffusion, and extract a pipe diffusion energy barrier that is larger than the energy barrier extracted from experimental data from hydrogen in deformed palladium. This analysis is not sufficient to explain the unusual jump distances extracted from experimental data. Chapter 3 focuses on calculat-

ing the incoherent scattering function. Quasielastic neutron scattering experiments of hydrogen in palladium measure incoherent scattering function over a range of energies for different magnitudes of the wavevector. We calculate the incoherent scattering function from our *ab initio* data, which allows us to comment on the current method of analyzing the experimental data. By mimicking the experimental analysis, we reproduce the unusual jump distances and find excellent agreement between the pipe diffusion barrier extracted using the experimental fitting procedure from our *ab initio* data and the pipe diffusion barrier extracted from experimental data. However, considering the incoherent scattering function restricts the comparisons of our simulations with experiment to data from a single instrument and does not allow for direct comparison of the scattering function itself. In chapter 4, we calculate the self-part of the intermediate scattering function again using our *ab initio* data as input. The calculation of the self part of the intermediate scattering function allows us to directly compare our simulations with experimental data from two instruments that cover a wider range of energies (times) than the energy (time) range accessible to a single instrument. Finally in chapter 5, we summarize our work, highlight the approximations in our model, and outline future areas of interest.

# CHAPTER 2

# HYDROGEN DIFFUSION

## 2.1 Introduction

Dislocations are carriers of plastic deformation, where planes of atoms slide past each other[106]. The theoretical critical shear stress is the stress required to slip an entire plane of atoms simultaneously. The stress required to plastically deform a material is much lower than the theoretical critical shear stress[107]. This overestimation of the critical shear stress gave rise to the idea of dislocations, where a line of atoms in the moving plane pushed into and displaced an adjacent row of atoms, and this motion continued until the entire plane was slipped. Dislocations were theorized as early as 1934[107–109] and were observed for the first time in 1953 via the segregation of silver to dislocations in silver bromide[110].

An edge dislocation introduces volumetric strain into a crystalline lattice. The atoms in the crystal experience compressive strain on the side of the slip plane that contains the extra half plane of atoms and tensile strain on the other side of the slip plane. The lattice strain field from a dislocation can attract other defects[111], influence the diffusion of defects[112, 113], and be influenced by their diffusion[114]. A Cottrell atmosphere[115] forms when the defects accumulate near a dislocation and create a pinning force, which increases the yield strength of a material. Lattice strain has been predicted to have a dramatic effect on the diffusion of hydrogen in palladium[116].

We study hydrogen diffusion in bulk palladium and near a dislocation. We choose to investigate an edge dislocation because edge dislocations, as opposed to screw dislocations, create volumetric strain in the crystal. For an fcc crystal, the close-packed planes are $\{111\}$ and the close-packed directions are $\langle 110 \rangle$. The slip planes for an edge dislocation are the close-packed planes in the

crystal, and the slip directions are the close-packed directions. We consider an $\frac{a}{2}[110](1\bar{1}\bar{1})$ edge dislocation. In Sect. 2.2 we use density functional theory to calculate site energies and diffusion barriers, from which we identify low energy pathways. Sect. 2.3 outlines our kinetic Monte Carlo simulation set up, which we use to compute diffusivities. Sect. 2.4 discusses our conclusions from these simulations.

## 2.2 Site energies, jump vectors, and jump rates

We perform DFT calculations using the plane-wave basis code VASP[117, 118]. We use projector augmented wave (PAW) potentials[119] generated by Kresse[120] with *s* valence for hydrogen, *s* and *d* valence electronic configurations for palladium, and the local density approximation for the exchange-correlation energy. For the dislocation geometry, we use a plane-wave energy cutoff of 250 eV, a $1 \times 1 \times 8$ *k*-point grid, a Methfessel-Paxton smearing width of 0.25 eV, and a force convergence of 5 meV/Å. These settings are identical to those chosen by Lawler and Trinkle[121] and Trinkle *et al.*[45] for simulating hydrogen near a palladium edge dislocation. For our calculations of site energies and energy barriers in the dislocation geometry, we keep the positions of palladium atoms in the outer region (c.f. Fig. 2.1) fixed and relax the positions of the inner region of palladium atoms and the hydrogen atom. For hydrogen in bulk palladium, we use a $6 \times 6 \times 6$ *k*-point grid and an energy cut off of 300 eV for our supercell containing 256 palladium atoms and one H interstitial. We calculate the equilibrium lattice parameter $a$ to be 3.852Å, which is slightly smaller than the experimental value of 3.872Å at 4.2K[34]. Previous DFT studies[38] found that hydrogen in bulk palladium diffuses from a ground state octahedral site to a tetrahedral site into another octahedral site. We perform climbing image nudged elastic band[122] calculations with a single image to compute the configurations and energies of the transition states. Our DFT calculated activation energy $E_{\mathrm{OT}} = 0.277$ eV for a hydrogen interstitial to transition from an octahedral site to a tetrahedral site in bulk palladium agrees well with the experimental value 0.230 eV[123].

An edge dislocation volumetrically strains interstitial sites near the dislocation core, which

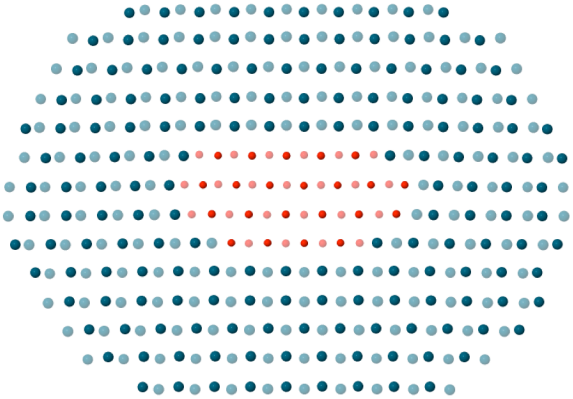

Figure 2.1: Fixed and relaxed regions of palladium atoms. The colored circles represent palladium atoms. The blue colored palladium atoms make up the outer region of atoms, which we hold fixed. We allow displacements for only the red colored palladium atoms and the hydrogen atom. The lighter and darker shades represent different atomic layers along the threading direction.

leads to lower diffusion barriers between expanded sites in palladium. We use a 382-atom palladium edge dislocation geometry with a [110] Burgers vector that is periodic along the $[1\bar{1}2]$ threading direction. The palladium edge dislocation geometry is the same as in Refs. [121] and [45]. We define the site energies of the interstitial sites in the dislocation relative to bulk as

$$E_{\text{interstitial}} = E_{\text{disl+H}} - E_{\text{disl}} - (E_{\text{bulk+H}} - E_{\text{bulk}}) \tag{2.1}$$

where $E_{\text{disl+H}}$ is the total energy of the dislocation supercell when the hydrogen atom is in an interstitial site, $E_{\text{disl}}$ is the energy of the dislocation without hydrogen, $E_{\text{bulk+H}}$ is the total energy of the bulk supercell with hydrogen in an interstitial site, and $E_{\text{bulk}}$ is the energy of bulk palladium without hydrogen. The ground state of hydrogen in the dislocation geometry is an octahedral site directly below the partial core, which has a site energy of $-0.125$ eV relative to an octahedral site in bulk[71]. We expect lowered barriers and thus accelerated diffusion in expanded sites below the partial core. While we do find a pathway with lower barriers below the partial core, the barrier to diffuse along this path, 0.151 eV, is higher than observed in experiment[71], $0.083 \pm 0.005$ eV for a hydrogen concentration of $1.13 \times 10^{-3}$ and $0.042 \pm 0.012$ eV for a hydrogen concentration of $0.52 \times 10^{-3}$. In addition to the low energy path below the partial core, we find a novel pathway

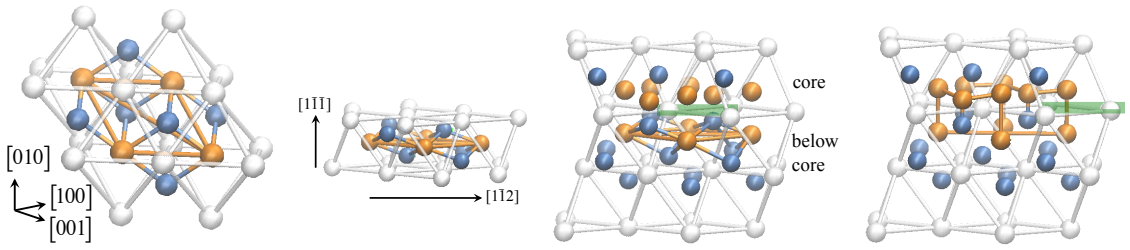


Figure 2.2: Geometries of hydrogen diffusion pathways. (a) The network for hydrogen diffusion between two octahedral interstitial sites (orange) along the [1$\bar{1}$2]-direction in fcc palladium includes two additional nearest neighbor octahedral interstitial sites along ⟨110⟩-type directions and six tetrahedral interstitial sites (blue). (b) The bulk network reoriented with the threading direction and slip plane normal of the edge dislocation shown. (c) The (partial) dislocation maintains periodicity along the [1$\bar{1}$2] threading direction. The network connecting two nearest neighbor octahedral sites along the [1$\bar{1}$2]-direction of the dislocation supercell in the expanded region directly below the partial core looks similar to the bulk network. The green slip plane is (1$\bar{1}\bar{1}$). (d) The lowest energy pathway through the periodic direction of the dislocation lies in the core of the partial dislocation. Here the distinction between octahedral and tetrahedral sites becomes blurred. The orange sites have low site energies—similar to octahedral sites—and the blue sites have high site energies—similar to tetrahedral sites.

inside the partial core (c.f. Fig. 2.2) with a lower barrier of 0.111 eV. However, this barrier is still higher than those measured by experiment.

Fig. 2.2 compares hydrogen diffusion paths along the [1$\bar{1}$2] threading direction directly below (Fig. 2.2(c)) and inside the dislocation partial core (Fig. 2.2(d)) to a diffusion path along the same direction in bulk palladium (Fig. 2.2(a)). The path below the partial core is expanded but still looks bulk-like. The highly distorted pathway inside the partial cores looks significantly different than the bulk pathway. The two $\frac{a}{6}\langle 211\rangle$ partial cores separate the face centered cubic structure outside the core region from the hexagonal close packed structure in the stacking fault. This transition between structures creates sheared sites in the partial cores that are neither octahedral nor tetrahedral. While some sites in the core become unstable or have high site energies, most of the sites have energies $\sim 0.03 - 0.06$ eV above the ground state. Diffusion pathways through these sites along the threading direction do not pass through higher energy tetrahedral sites as they do in the bulk. The barriers to diffuse from the expanded region below the core into the core are low, as small as 0.048 eV, while the barrier out of the core is 0.041 eV.

Fig. 2.3 compares the spatial distributions of volumetric strain due to the dislocation for octahedral and tetrahedral interstitial sites that lead to inhomogeneous changes in the relative site energies and energy barriers between the differently strained sites. We use the volumetric strain to approximate the site energies and energy barriers away from the dislocation core. To evaluate the volumetric strain, we first identify the six (four) palladium atoms that define the octahedral (tetrahedral) "cage"; then, we take the center of mass of the cage as the interstitial site, and use the vectors from this site to the neighbors to find the volumetric strain[124]. The extra half plane creates compressive strain above the slip plane and tensile strain below the slip plane for both octahedral and tetrahedral sites. Sites near the partial cores have the largest volumetric strain, with the strain falling off more quickly for the tetrahedral sites than for the octahedral sites. There are only two site energies ($E_{\mathrm{O}}$ and $E_{\mathrm{T}}$) and two barriers in bulk ($E_{\mathrm{OT}}$ and $E_{\mathrm{TO}}$), but the dislocation breaks the symmetry, leading to spatially dependent site energies and barriers. We use DFT to calculate the energetics of hydrogen in highly distorted sites inside the stacking fault, inside the dislocation partial cores, and below the partial cores. However, calculating each site energy and site energy barrier in the dislocation geometry with DFT is computationally expensive, so we develop an approximation for the site energies and energy barriers for sites outside of the partial dislocation cores using the volumetric strains.

Fig. 2.4 shows the distribution of $E_{\mathrm{OT}}$ barriers relative to the bulk $E_{\mathrm{OT}}$ barrier. The barrier to diffuse in bulk palladium is the $E_{\mathrm{OT}}$ barrier, as the $E_{\mathrm{TO}}$ barrier is much smaller. The compressive region of the dislocation geometry leads to higher $E_{\mathrm{OT}}$ barriers, while the tensile region leads to lower barriers. One would expect that the lower diffusion barriers in the expanded region below the partial cores will lead to faster diffusion along the threading direction. In addition, the lower energy pathway inside the core and stacking fault between highly distorted interstitial sites should contribute to accelerated diffusion.

Fig. 2.5 shows the linear relationships between energy and small volumetric strains in bulk that we use to model site energies and energy barriers around the dislocation geometry. We calculate site energies of hydrogen in unstrained and ±2% strained bulk using DFT. We find the site energy

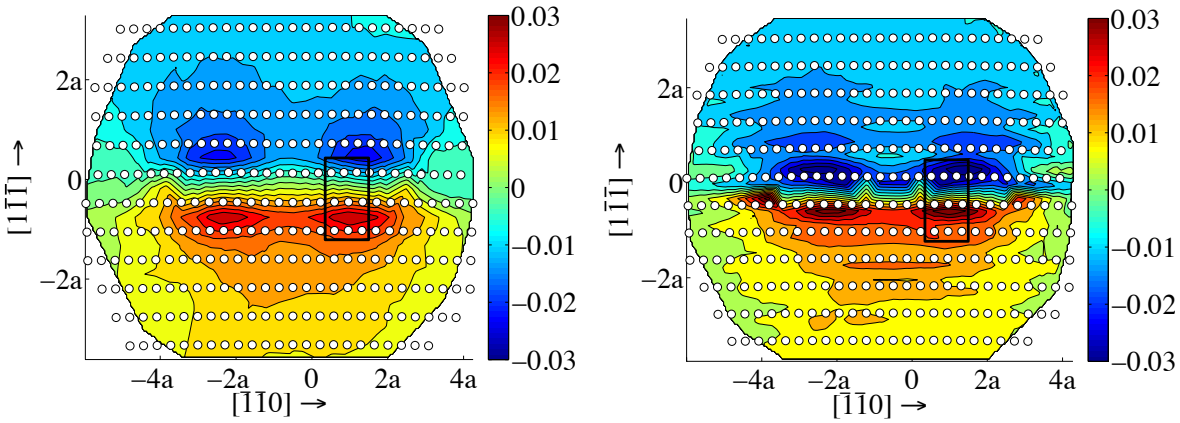


(a) Octahedral sites (b) Tetrahedral sites

Figure 2.3: Volumetric strain of (a) octahedral interstitial and (b) tetrahedral interstitial sites in an $\frac{a}{2}$[110] edge dislocation that has split into partials. The extra half plane is located on the top half of the figure, and the Burgers vector points along [110]. The black boxes outline the palladium atoms and interstitial sites included in Fig. 2.2(c) and 2.2(d). The dislocation geometry is periodic along the [1$\bar{1}$2] threading direction, pointing out of the page (in contrast to Fig. 2.2(c) and 2.2(d), in which the threading direction points to the right). This dislocation has split into two partials in the (1$\bar{1}\bar{1}$) slip plane. The sites with the largest tensile (positive) strain are located beneath the partial cores.

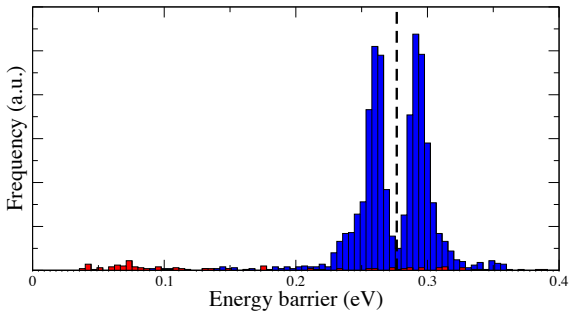


Figure 2.4: Distribution of energy barriers. The dashed line marks the $E_{\mathrm{OT}}$ in bulk. The bimodal distribution near the bulk $E_{\mathrm{OT}}$ value corresponds to the $E_{\mathrm{OT}}$ barriers in the compressive and tensile regions that are, as expected, larger and smaller than the bulk value. The lowest energy barriers, in red, correspond to barriers between distorted sites in the dislocation core that are neither octahedral nor tetrahedral.

difference

$$E_{\mathrm{T}}(\varepsilon_{\mathrm{V}}) - E_{\mathrm{O}}(\varepsilon_{\mathrm{V}}) = 0.152\ \mathrm{eV} - (1.70\ \mathrm{eV})\varepsilon_{\mathrm{V}}, \tag{2.2}$$

the octahedral to tetrahedral diffusion barrier

$$E_{\mathrm{OT}}(\varepsilon_{\mathrm{V}}) = 0.277\ \mathrm{eV} - (1.82\ \mathrm{eV})\varepsilon_{\mathrm{V}}, \tag{2.3}$$

and the tetrahedral to octahedral diffusion barrier

$$E_{\mathrm{TO}}(\varepsilon_{\mathrm{V}}) = 0.125\ \mathrm{eV} - (0.128\ \mathrm{eV})\varepsilon_{\mathrm{V}}, \tag{2.4}$$

where $\varepsilon_{\mathrm{V}}$ is the volumetric strain. The linear change in the site energy difference and energy barrier with respect to strain, in the small strain limit ($\pm 2\%$) in bulk, is consistent with previous studies[116]. We compare the site energies calculated with DFT and the approximated site energies for the outermost sites of the expanded region and find good agreement to within 25 meV, which justifies our use of this simple approximation. The transition state—located in a {111} face—is two-thirds along the line from octahedral to tetrahedral sites. If we consider octahedral and tetrahedral sites that have different strains, we model the energy barriers as

$$E_{\mathrm{OT}}^{\mathrm{hetero}}(\varepsilon_{\mathrm{O}}, \varepsilon_{\mathrm{T}}) = \frac{2}{3}[E_{\mathrm{T}}(\varepsilon_{\mathrm{T}}) - E_{\mathrm{O}}(\varepsilon_{\mathrm{O}})] + \frac{1}{3}E_{\mathrm{OT}}\left(\frac{\varepsilon_{\mathrm{T}} + \varepsilon_{\mathrm{O}}}{2}\right) + \frac{2}{3}E_{\mathrm{TO}}\left(\frac{\varepsilon_{\mathrm{T}} + \varepsilon_{\mathrm{O}}}{2}\right) \tag{2.5}$$

and

$$E_{\mathrm{TO}}^{\mathrm{hetero}}(\varepsilon_{\mathrm{O}}, \varepsilon_{\mathrm{T}}) = -\frac{1}{3}[E_{\mathrm{T}}(\varepsilon_{\mathrm{T}}) - E_{\mathrm{O}}(\varepsilon_{\mathrm{O}})] + \frac{1}{3}E_{\mathrm{OT}}\left(\frac{\varepsilon_{\mathrm{T}} + \varepsilon_{\mathrm{O}}}{2}\right) + \frac{2}{3}E_{\mathrm{TO}}\left(\frac{\varepsilon_{\mathrm{T}} + \varepsilon_{\mathrm{O}}}{2}\right), \tag{2.6}$$

where we use the average of the volumetric strain of the octahedral site $\varepsilon_{\mathrm{O}}$ and the volumetric strain of the tetrahedral site $\varepsilon_{\mathrm{T}}$ as the strain of the transition state. The factors of $\frac{1}{3}$ and $\frac{2}{3}$ come from the location of the transition state, which is $\frac{2}{3}$ of the distance from the O site to the T site. We use a constant prefactor $\nu_0 = 10^{13}\ \mathrm{s}^{-1}$ to compute the jump rate $\nu_{mn} = \nu_0 \exp(-E_{mn}/k_{\mathrm{B}}T)$ from site $m$ to site $n$.

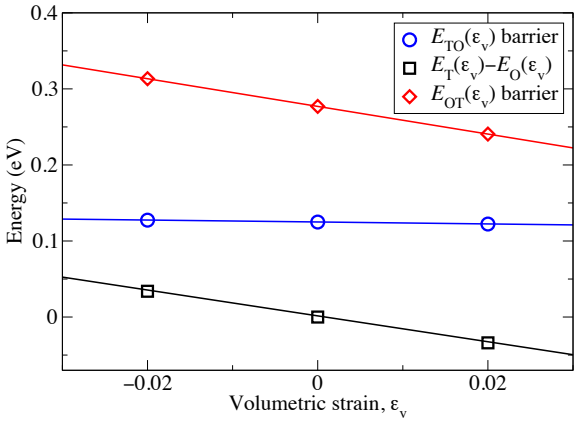


Figure 2.5: Strain dependence of bulk octahedral to tetrahedral energy barrier, tetrahedral to octahedral energy barrier, and octahedral and tetrahedral site energy difference. For small strains, site energies and energy barriers computed with DFT vary linearly with respect to strain. The individual site energy differences also vary linearly with respect to strain. We use these simple linear strain dependencies to approximate the site energies and energy barriers for all sites in the dislocation geometry, excluding the highly distorted sites and barriers inside the partial cores and in the stacking fault.

## 2.3 Kinetic Monte Carlo

Monte Carlo algorithms are based on the generation of random numbers. Metropolis Monte Carlo[125] is the most well known Monte Carlo algorithm. The Metropolis algorithm samples the states of a system and can be used to determine statistical averages over configurations. This algorithm allows for unphysical transitions to take place, which leads to more efficient sampling of equilibrium properties but precludes the study of dynamical processes. Later, the kinetic Monte Carlo (KMC) algorithm[126] became a popular method for studying the evolution of systems governed by rare events. Kinetic Monte Carlo simulations simplify the system by only partitioning the system into a discrete set of states with transition rates between connected states. The KMC algorithm uses random numbers to select transitions and determine the waiting time between transitions. The KMC time is pulled from an exponential distribution. The downside to KMC simulations is that the simulations require prior knowledge of the connectivity of all of the sites as well as the escape rates.

Fig. 2.6 compares the results of KMC simulations with an analytical solution for diffusion of

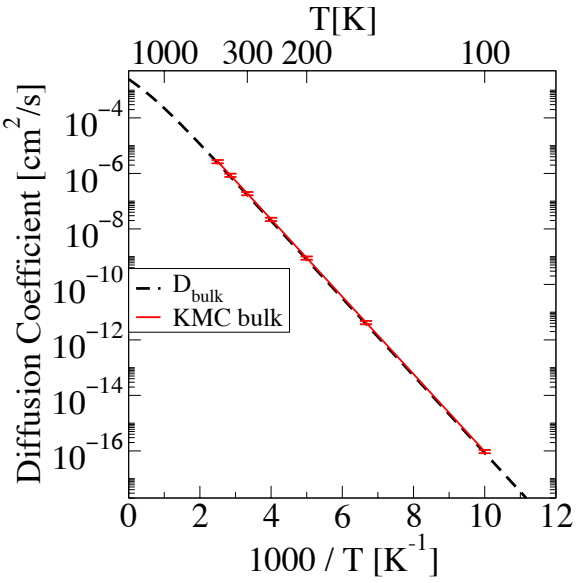


Figure 2.6: Bulk diffusion of hydrogen in palladium. The diffusivity calculated from KMC simulations agrees well with the analytical solution. The error bar for each temperature is the error of the mean.

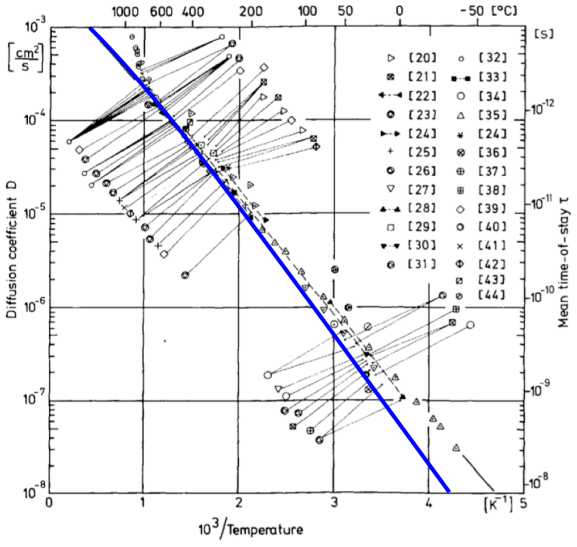


Figure 2.7: Comparison of bulk analytical expression with experimental data. The diffusion barrier from our *ab initio* calculations is larger than the diffusion barrier extracted from experiments[123]. However, we find excellent agreement between our predicted diffusion coefficient and the experimentally measured values for temperatures around 400–1000 K.

hydrogen in bulk palladium. For the diffusion of hydrogen in bulk palladium, we can derive an analytical expression from the multi-state diffusion formalism[127]

$$D = \frac{a^2}{2}\left(\frac{\nu_{\mathrm{OT}}\nu_{\mathrm{TO}}}{2\nu_{\mathrm{OT}} + \nu_{\mathrm{TO}}}\right). \tag{2.7}$$

Fig. 2.7 shows that this analytical model agrees well with the available experimental data.However as the number of sites in the geometry increases, this analytical expression becomes complicated[128]. In anticipation of analyzing a dislocation geometry with its large number of sites, we also use atomic scale simulations to calculate diffusion. In contrast to molecular dynamics, which spends the majority of the simulation time in local minima and only occasionally crosses over barriers to new states, KMC effectively simulates rare events. We use a single palladium atom unit cell containing one octahedral site and two tetrahedral sites with periodic boundary conditions and a single hydrogen atom for our bulk KMC simulations. The hydrogen atom has no interaction with its periodic images so that our simulations model an infinitely dilute concentration of hydrogen. The initial position of the hydrogen atom is randomly chosen with the probability of each site set according to the Boltzmann probability distribution of the site energies. The average diffusivity values and error bars are evaluated from 3000 KMC trajectories each with $10^4$ steps. We find excellent agreement between the diffusivity of hydrogen in bulk palladium calculated from our KMC simulations to the analytical solution.

Fig. 2.8 shows faster diffusion along the threading direction than perpendicular to the threading direction for sample trajectories at 100K, 300K, and 500K. We use the jump rates along with the site energies and jump vectors from the dislocation geometry described in Sect. 2.2 as input for KMC calculations. We run trajectories with $10^4$ transitions unless the hydrogen atom jumps outside of the dislocation geometry, at which point we consider it to have escaped. At 100K, all trajectories have a length of $10^4$ transitions, because the hydrogen atom never escapes the dislocation. The trapping of the hydrogen to the dislocation can be seen as a leveling off in the $r^2$-value perpendicular to the threading direction for 100K. As temperature increases, the percentage

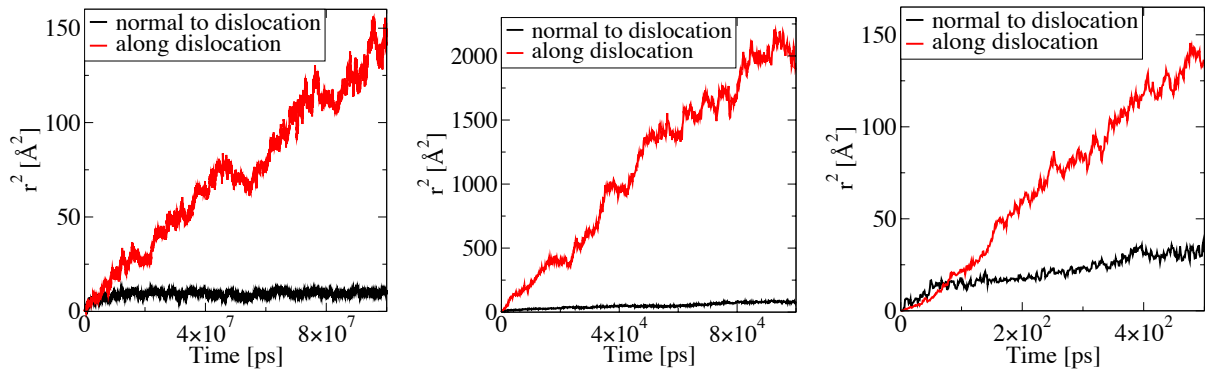


(a) 100K (b) 300K (c) 500K

Figure 2.8: Distance travelled by the hydrogen atom along the threading vector and perpendicular to the threading vector versus time. The hydrogen atom moves farther along the threading direction than in the plane perpendicular to the threading direction over the same amount of time. Note that as temperature increases, the simulation time range decreases.

of trajectories for which the hydrogen atom jumps outside of the dislocation supercell increases.

Fig. 2.9 shows a reduced activation barrier for diffusion relative to the barrier in bulk. For each temperature, we average 3000 KMC trajectories and calculate diffusivity from the long time limit of the mean squared displacement divided by time. From the computed diffusivities over the temperature range 100–500 K, we extract an effective activation barrier for diffusion of $E_a$ = 0.125 eV; this is larger than the experimentally modeled activation barrier of 0.042–0.083 eV, extracted from a Chudley-Elliot analysis of incoherent scattering[71]. The deviation from linearity at higher temperatures in the Arrhenius plot indicates changes in the diffusion mechanism as pipe diffusion becomes less dominant at higher temperatures.

## 2.4 Conclusion

We use DFT site energy and energy barrier calculations to find that hydrogen binds to low energy sites below the dislocation core and experiences reduced activation barriers in the expanded region below the core. We also find a lower energy pathway inside the dislocation core. Kinetic Monte Carlo simulations provide evidence for pipe diffusion. In addition, KMC simulations do not predict unusual changes in average jump distance with temperature, as the Chudley-Elliot analysis

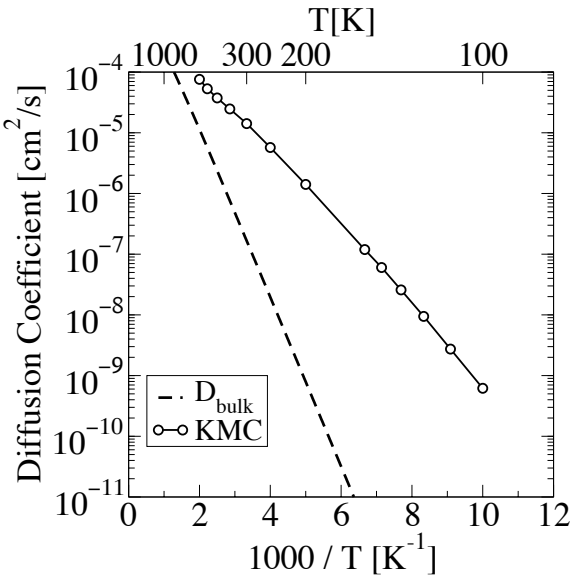


Figure 2.9: Hydrogen diffusion along the threading direction in the dislocation geometry. The error bar for each temperature is smaller than the symbol size. We show the analytical solution for bulk diffusion (dashed line) for comparison.

suggests[71]; to explain these discrepancies, we compute the incoherent scattering function.

# CHAPTER 3

# INCOHERENT SCATTERING

## 3.1 Introduction

Incoherent QENS experiments measure long range particle diffusion[78]. The interpretation of QENS data is challenging. In general, the data is fit with an analytical model with adjustable parameters. One common analytical model is the Chudley-Elliott model based on diffusion in an isotropic material[73]. The parameters of such models can then be compared with *ab initio* data[71, 129]. A more direct comparison between simulations and QENS data requires the calculation of the incoherent scattering function.

A number of studies have highlighted difficulties in calculating the incoherent scattering function. Li and Wahnström used molecular dynamics with an embedded-atom method potential to calculate the intermediate scattering function from the self-correlation function for hydrogen in bulk palladium[130, 131]. Comparison with experimental results required a temporal Fourier transform of the intermediate scattering function to produce the incoherent scattering function. The authors transformed the intermediate scattering function by introduced a dampening factor with an adjustable parameter to smooth out the intermediate scattering function. These authors introduced an adjustable parameter friction coefficient based on first principles calculations of hydrogen in a homogeneous electron gas[131] to better match experimental results[93]. Gillan used a similar approach for hydrogen in palladium using a pair potential and also failed to find agreement with experiment[132]. Björketun *et al.* used DFT-informed KMC simulations to calculate incoherent scattering of a proton in a disordered perovskite structure but failed to recover the expected $Q^2$ law for small $Q$[92]. Rowe *et al.* developed an analytical solution for diffusion through

a network of energetically equivalent octahedral and tetrahedral sites in a body centered cubic lattice[89]. Building upon this method, Kehr *et al.* computed the incoherent scattering function for one-dimensional lattices with inequivalent site energies[133]. A generalized version of this method has been developed to calculate the incoherent scattering function from an arbitrary diffusion network[78, 134–136], but this approach has not been applied to study hydrogen diffusion near a dislocation.

We use DFT to compute site energies and energy barriers of hydrogen in a palladium edge dislocation geometry from which we calculate the incoherent scattering function using the generalized analytic method mentioned above. We consider only an edge dislocation, as it has the strongest binding with hydrogen, and hence, at low concentrations and temperatures, produce the dominant signal. The analysis allows for direct comparison with QENS data[71]. We also follow the same fitting procedures as a typical QENS experiment[137] by fitting the incoherent scattering function versus energy to a single Lorentzian, extracting the half-width-at-half-maximum, and fitting these widths as a function of $Q$ to a CE model, Eqn. (1.7).We calculate the diffusivity from the parameters of the CE model using Eqn. (1.8). We try several fitting schemes of a single Lorentzian to the simulated incoherent scattering function, and each produces different values for diffusivities and jump distances. We find that the typical fitting procedure introduces unphysical jump distances and underestimates the diffusion barrier along the dislocation.

## 3.2 Evaluating the incoherent scattering function

We construct the incoherent scattering function from site energies, jump rates, and jump vectors of the diffusion network to compare with quasielastic neutron experiments. A generalized expression for incoherent scattering is derived in Ref. [78]; we outline this derivation below. The jump matrix $\Lambda$ in reciprocal space is

$$\Lambda_{mn}(\mathbf{Q}) = \nu_{mn} \exp(i\mathbf{Q} \cdot \mathbf{s}_{nm}) - \delta_{mn} \sum_{l \neq n} \nu_{nl}, \tag{3.1}$$

where $\nu_{mn}$ is the jump rate from site $m$ to $n$, $\mathbf{Q}$ is the wavevector, $\delta_{mn}$ is the Kronecker delta, and $\mathbf{s}_{nm}$ is the jump vector from site $n$ to site $m$. The neutron will transfer momentum to the hydrogen atom, corresponding to $\mathbf{Q}$. With the site probabilities $\rho_n = \exp(-\beta E_n)/\sum_m \exp(-\beta E_m)$, we construct a Hermitian jump matrix,

$$\tilde{\Lambda}(\mathbf{Q}) = \rho^{-\frac{1}{2}} \Lambda(\mathbf{Q}) \rho^{\frac{1}{2}}, \tag{3.2}$$

where $\rho^{\frac{1}{2}}$ is a diagonal matrix of the square root of site probabilities. The jump matrix is negative definite, and its eigenvalues are negative. The incoherent scattering function is a sum of Lorentzians whose widths and weights are given be the eigenvalues $\tilde{\lambda}_i(\mathbf{Q})$ and eigenvectors $\tilde{e}_i(\mathbf{Q})$ of the Hermitian jump matrix $\tilde{\Lambda}(\mathbf{Q})$,

$$S_{\text{inc}}(\mathbf{Q}, \omega) = \frac{1}{\pi} \sum_{i=1}^{N_{\text{sites}}} w_i(\mathbf{Q}) \frac{-\hbar\tilde{\lambda}_i(\mathbf{Q})}{(\hbar\tilde{\lambda}_i(\mathbf{Q}))^2 + (\hbar\omega)^2}, \tag{3.3}$$

where the weights $w_i(\mathbf{Q})$ are

$$w_i(\mathbf{Q}) = \sum_{l}^{N_{\text{sites}}} \sum_{n}^{N_{\text{sites}}} \rho_l^{\frac{1}{2}} \tilde{e}_{in}(\mathbf{Q}) \tilde{e}^*_{il}(\mathbf{Q}) \rho_n^{\frac{1}{2}} = \left| \sum_{l}^{N_{\text{sites}}} \rho_l^{\frac{1}{2}} \tilde{e}_{il}(\mathbf{Q}) \right|^2. \tag{3.4}$$

The curvature of the incoherent scattering function $S_{\text{inc}}(\mathbf{Q}, \omega)$ gives the diffusivity at the small $Q$ limit. When the diffusion occurs on a Bravais lattice, Eqn. (3.3) simplifies to a single Lorentzian with a width $\tilde{\lambda}(\mathbf{Q})$. Eqn. (3.3) captures the full anisotropy of the scattering function; however, experiments on polycrystalline samples produce a spherically averaged $S_{\text{inc}}(\mathbf{Q}, \omega)$

$$S_{\text{inc}}(Q, \omega) = \iint_{4\pi} \frac{d^2\hat{\mathbf{Q}}}{4\pi} S_{\text{inc}}(Q\hat{\mathbf{Q}}, \omega). \tag{3.5}$$

We numerically evaluate $S_{\text{inc}}(\mathbf{Q}, \omega)$ on a spherical grid of points to compute the spherical average. We use uniformly spaced points for $\phi$ from 0 to $2\pi$. For $\theta$, we use one-dimensional Gauss quadrature, specifically Gauss-Legendre nodes with weights $c_i$[138]. The Gauss-Legendre nodes span the interval $[-1, 1]$. We take the inverse cosine of the nodes to get $\theta$ points that span 0 to $\pi$. Our

expression for the approximate integral is

$$S_{\text{inc}}(Q,\omega) \approx \frac{1}{N_\phi} \sum_{j=1}^{N_\phi} \sum_{i=1}^{N_\theta} c_i \cdot S_{\text{inc}}(\mathbf{Q}(\theta_i, \phi_j), \omega), \tag{3.6}$$

where $N_\theta$ and $N_\phi$ are the number of grid points. The final result is an incoherent scattering function that can be written as an integral of Lorentzians,

$$S_{\text{inc}}(Q,\omega) = \int_0^\infty d\lambda \; W(Q;\lambda) \frac{1}{\pi} \frac{\hbar\lambda}{(\hbar\lambda)^2 + (\hbar\omega)^2} \tag{3.7}$$

for a normalized "density of rates" $W(Q;\lambda)$. If our scattering function were represented by a Lorentzian with one width, $W$ would be a delta function; however, we find a non-trivial distribution of rates that can only be approximated by a simple Lorentzian fit.

## 3.3 Analyzing the incoherent scattering function

### 3.3.1 Bulk

Fig. 3.1 shows that the CE model does not capture the behavior of spherically averaged incoherent scattering function $S_{\text{inc}}(Q,\omega)$ even for hydrogen in bulk palladium. The spherically averaged $S_{\text{inc}}(Q,\omega)$ converges with a coarse $10 \times 10$ mesh of points on the sphere, but for the purpose of plotting the density of rates of $S_{\text{inc}}(Q,\omega)$ we use a finer $100 \times 100$ mesh. We compare the density of rates of $S_{\text{inc}}(Q,\omega)$ to the CE model, which assumes an isotropic jump distance and a single jump rate (or inverse mean residency time). The octahedral sites make up a Bravais lattice, but the network of octahedral and tetrahedral sites is not a Bravais lattice. The corresponding CE model uses the jump distance between octahedral sites and jump rate between octahedral sites, which is 3/4 the jump rate between an octahedral and a tetrahedral site when the tetrahedral site has a short residency time. At small $Q$, the density of rates of $S_{\text{inc}}(Q,\omega)$ is well-represented by the CE curve, which is why CE gives accurate diffusivity for bulk. However, at large $Q$ the CE

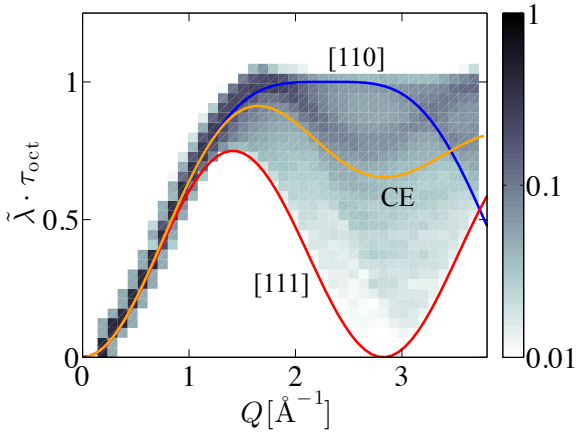


Figure 3.1: Density of rates $W(Q;\lambda)$ of $S_{\text{inc}}(Q,\omega)$ for H in bulk Pd at 100K. The grey scale indicates the weight of Lorentzian terms of widths (rates) $\tilde{\lambda}$ within a histogram bin; the sum of all weights for each $Q$ is normalized to one. The widths are reported relative to the mean residency time in bulk, $\tau_{\text{oct}}$. At small $Q$, a single width has a weight close to one because $S_{\text{inc}}(\mathbf{Q},\omega)$ is the same along all directions. At larger $Q$, the $\mathbf{Q}$-directional dependence of $S_{\text{inc}}(\mathbf{Q},\omega)$ produces a range of rates with non-negligible weights. The Chudley-Elliott (CE) model cannot fully capture this spread in the density of rates of the spherically averaged scattering function $S_{\text{inc}}(Q,\omega)$. Scattering with $\mathbf{Q}$ along [111], which connects octahedral and tetrahedral sites, gives the lower bound of the distribution. Scattering with $\mathbf{Q}$ along [110], which connects nearest neighbor octahedral sites, corresponds to relatively high weights.

curve cannot capture the spread in the density of rates of $S_{\text{inc}}(Q,\omega)$. We compare the density of rates of $S_{\text{inc}}(Q,\omega)$ with analytic solutions for $S_{\text{inc}}(\mathbf{Q},\omega)$ along particular directions. The spread in the density of rates of $S_{\text{inc}}(Q,\omega)$ is bounded below by scattering along [111]-type directions, which connects neighboring octahedral and tetrahedral sites. Lorentzian terms corresponding to scattering along [110]-type directions, which connects nearest neighbor octahedral sites, have large weights. The dark band above the CE curve does not correspond to scattering along a single direction but has contributions from several different directions.

### 3.3.2 Dislocation

We fit $S_{\text{inc}}(Q,\omega)$ with a single Lorentzian and use the CE model to investigate the validity of the experimentally measured jump distances and diffusivities. We try four different fitting approaches. Since the weights sum to one, the most straightforward approach is fitting a single Lorentzian with

a width equal to the weighted average of the widths of the Lorentzians that make up $S_{\text{inc}}(Q,\omega)$,

$$\bar{\lambda} = \sum_i w_i \lambda_i. \tag{3.8}$$

This fit matches exactly for $\omega \to \infty$. The second approach is fitting a single Lorentzian of width $\Gamma$ that minimizes the difference between the exact $S_{\text{inc}}(Q,\omega)$ and the single Lorentzian, i.e. the fit minimizes

$$\chi^2_{[0,\infty]} = \int_0^\infty \left(S_{\text{inc}}(\mathbf{Q},\omega) - \frac{\Gamma}{\pi(\Gamma^2+\omega^2)}\right)^2 d\omega. \tag{3.9}$$

We denote the width that minimizes this error as $\Gamma_{[0,\infty]}$. This fit favors smaller widths than the weighted average. Weighting the integrand by $\omega^2$ gives

$$\chi^2_{\omega^2,[0,\infty]} = \int_0^\infty \omega^2 \cdot \left(S_{\text{inc}}(\mathbf{Q},\omega) - \frac{\Gamma}{\pi(\Gamma^2+\omega^2)}\right)^2 d\omega, \tag{3.10}$$

where terms corresponding to higher frequency contribute more to the error being minimized. We denote the width that minimizes this error as $\Gamma_{\omega^2,[0,\infty]}$. Compared to the weighted average fit, the fits obtained from $\chi^2_{[0,\infty]}$ and $\chi^2_{\omega^2,[0,\infty]}$ both favor terms with smaller widths. These three different fits have similar forms if we rewrite the equation for $\bar{\lambda}$ as

$$1 = \sum_i w_i \frac{2\lambda_i}{2\bar{\lambda}}, \tag{3.11}$$

the equation for $\Gamma_{[0,\infty]}$ as

$$1 = \sum_i w_i \left(\frac{2\Gamma_{[0,\infty]}}{\lambda_i + \Gamma_{[0,\infty]}}\right)^2, \tag{3.12}$$

and the equation for $\Gamma_{\omega^2,[0,\infty]}$ as

$$1 = \sum_i w_i \left(\frac{2\lambda_i}{\lambda_i + \Gamma_{\omega^2,[0,\infty]}}\right)^2. \tag{3.13}$$

A single Lorentzian would give identical widths for all fitting procedures, but a distribution of Lorentzians produces different widths for the different fits. If we consider a uniform distribution of eigenvalues that extends over a range that is twice the mean width, then $\bar{\lambda}$ equals the mean width, $\Gamma_{[0,\infty]}$ is $\frac{2}{3}\bar{\lambda}$, and $\Gamma_{\omega^2,[0,\infty]}$ is $0.9307\bar{\lambda}$. Thus, $\Gamma_{[0,\infty]} < \Gamma_{\omega^2,[0,\infty]} < \bar{\lambda}$. The distribution of eigenvalues and weights from the dislocation geometry are more complicated than a uniform distribution, so we also consider an experiment-like fit over a fixed range of energies.

Experiment cannot probe $S_{\text{inc}}(Q,\omega)$ for arbitrarily small or large energies or $Q$-magnitudes. The experimental resolution, $\pm 3.4$ $\mu$eV, and the experimental window, $\pm 100$ $\mu$eV,[71] limit the range of energies accessible in QENS experiments. Therefore, we also try a least squares fit over a fixed range. The $S_{\text{inc}}(Q,\omega)$ spectra are sums of Lorentzians that span multiple orders of magnitude. To avoid having just a few sharply peaked terms in $S_{\text{inc}}(Q,\omega)$ dominate the fit, we use a logarithmic least squares fit to $S_{\text{inc}}(Q,\omega)$,

$$\chi^2_{\log,[3.4,100]} = \int_{3.4\ \mu\text{eV}/\hbar}^{100\ \mu\text{eV}/\hbar} d\omega \left( \log\left(S_{\text{inc}}(Q,\omega)\right) - \log\left(\frac{\Gamma}{\pi(\Gamma^2+\omega^2)}\right)\right)^2, \tag{3.14}$$

over the same range as experimental measurements. As there isn't a closed-form analytic expression, we evaluate the integral using a quadrature with $N_\omega$ equally spaced $\omega$ values over the interval $[3.4, 100]$. We denote the width that minimizes this error as $\Gamma_{\log,[3.4,100]}$, and it is the fit that best represents the experimental analysis.

Fig. 3.2 shows that a Lorentzian of width $\Gamma_{\log,[3.4,100]}$ is the best fit to $S_{\text{inc}}(Q,\omega)$ in the range of experimentally accessible energies. At low temperatures, $\bar{\lambda}$ performs better than $\Gamma_{\omega^2,[0,\infty]}$, because many of the terms with large weights have widths that are smaller than the experimental resolution. Since $S_{\text{inc}}(Q,\omega)$ is sharply peaked at low temperatures, the range of experimentally accessible energies approaches the large $\hbar\omega$ limit where $\bar{\lambda}$ is exact. As temperature increases, $S_{\text{inc}}(Q,\omega)$ becomes less sharply peaked. At intermediate temperatures, $\Gamma_{\omega^2,[0,\infty]}$ becomes a better representation of the part of the function that falls within the experimentally observable range. Neither $\Gamma_{\omega^2,[0,\infty]}$ nor $\bar{\lambda}$ is a good fit within the experimentally observable range of $\hbar\omega$ for the entire

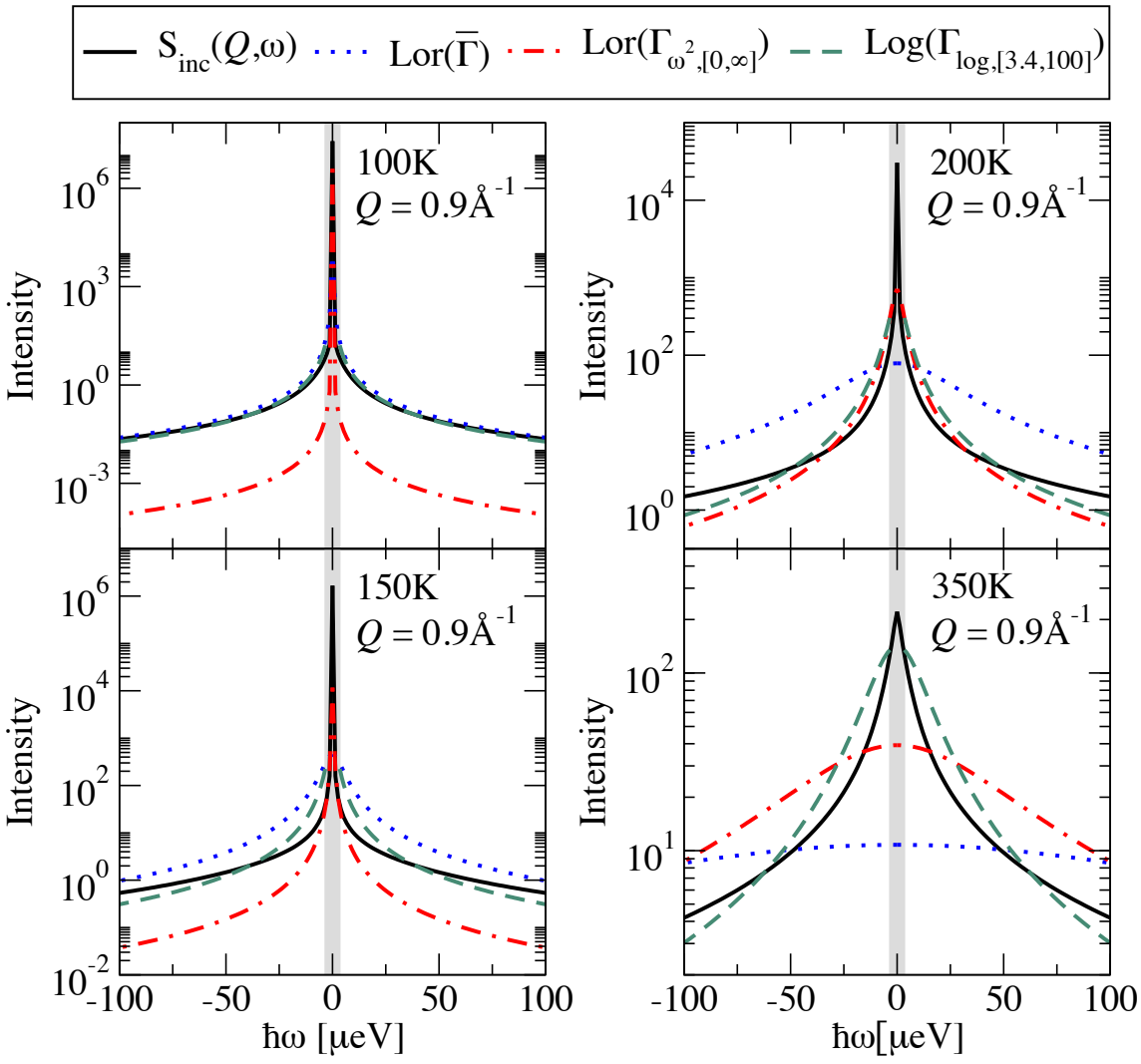


Figure 3.2: Single Lorentzian fits of the analytic $S_{\text{inc}}(Q,\omega)$ as a function of neutron energy $\hbar\omega$ for $Q = 0.9\text{Å}^{-1}$ at 100K, 150K, 200K, and 350K for the dislocation geometry. The range of $\hbar\omega$ plotted reflects the experimental window $\pm 100$ $\mu$eV, and the grey shading denotes energies smaller than the experimental resolution of $\pm 3.4$ $\mu$eV. The fit to $\bar{\lambda}$ is exact for $\hbar\omega \to \infty$, and well represents $S_{\text{inc}}(Q,\omega)$ at 100K, where the majority of the weight is distributed amongst terms with widths smaller than the experimental resolution. At higher temperatures, $\bar{\lambda}$ becomes a worse fit of $S_{\text{inc}}(Q,\omega)$ within the experimental window. The fit that minimizes $\chi^2_{\omega^2,[0,\infty]}$ favors smaller widths, which makes the fit poor in the range of experimentally accessible values at low temperatures. At high temperatures, both $\Gamma_{\omega^2,[0,\infty]}$ and $\bar{\lambda}$ appear to be too large in this range. The range of $\hbar\omega$ values over which $S_{\text{inc}}(Q,\omega)$ is plotted determines which of these two fits appears to be better fit. For all temperatures, the fit that minimizes $\chi^2_{\text{log},[3.4,100]}$, which is fit to only experimentally accessible $\hbar\omega$ values, appears to best describe $S_{\text{inc}}(Q,\omega)$ within the fixed experimental window.

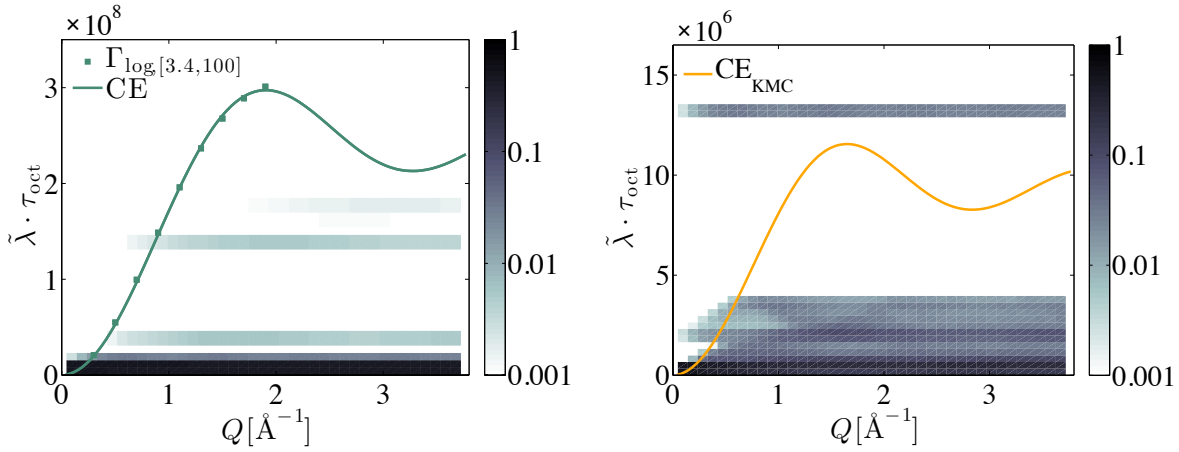


Figure 3.3: Density of rates $W(Q;\lambda)$ of $S_{\text{inc}}(Q,\omega)$ for the dislocation geometry at 100K. The grey scale indicates the weight of Lorentzian terms of widths (rates) $\tilde{\lambda}$ within a histogram bin; the sum of all weights for each $Q$ is normalized to one. The widths are reported relative to the mean residency time in bulk, $\tau_{\text{oct}}$. (Left) The symbols correspond to the fit widths $\Gamma_{\text{log},[3.4,100]}$ and the curve is the CE model fit to those widths as a function of $Q$. (Right) The curve is the CE model using the distance between bulk nearest neighbor octahedral sites as the jump distance and diffusivity from KMC simulations, so that the curvature matches the diffusivity; note the vertical scale is two orders of magnitude smaller. Unlike the bulk case in Fig. 3.1, there is no single width that represents the distribution of weights even at small Q. The majority of the weight for each $Q$ is distributed amongst eigenvalues that are much smaller than $\Gamma_{\text{log},[3.4,100]}$.

range of temperatures.

Fig. 3.3 and 3.4 show that neither $\Gamma_{\text{log},[3.4,100]}$ nor CE fits to $\Gamma_{\text{log},[3.4,100]}$ capture physical rates that dominate $S_{\text{inc}}(Q,\omega)$, but $\Gamma_{\text{log},[3.4,100]}$ matches well with the widths from experiment for deformed palladium. The spread of the density of rates of $S_{\text{inc}}(Q,\omega)$ for hydrogen in the dislocation cannot be captured by a single Lorentzian width even at small $Q$. At 100K, $\Gamma_{\text{log},[3.4,100]}$ is over an order of magnitude larger than the highest weighted widths. This corroborates with Fig. 3.2 that at low temperatures the widths with the largest weight are smaller than the experimental resolution and are not represented by $\Gamma_{\text{log},[3.4,100]}$. The CE model parametrized with the diffusivity from KMC and the distance between nearest neighboring octahedral sites in bulk spans a smaller range of widths that falls closer to the higher weighted widths. However, Fig. 3.3 shows that the spread in the density of rates of $S_{\text{inc}}(Q,\omega)$ cannot be described as a single width. The density of rates of $S_{\text{inc}}(Q,\omega)$ features large gaps between eigenvalues with large weights, because the spectrum of

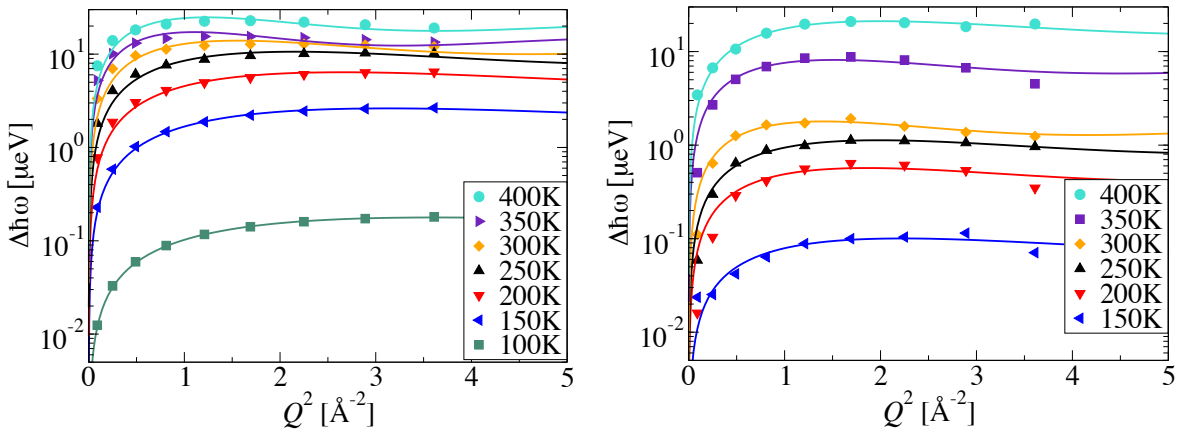


Figure 3.4: Chudley-Elliott fit to the widths of $S_{\text{inc}}(Q,\omega)$ for the dislocation geometry. (Left) The symbols correspond to $\Gamma_{\text{log},[3.4,100]}$ and the lines are CE fits to those widths for each temperature. The CE model captures the trend of the fitted widths as a function of $Q$. The widths from the least squares fit of $\log(S_{\text{inc}}(Q,\omega))$ vary across the same orders of magnitude for increasing temperatures as seen in experiment[71] (Right).

rates is not continuous. In bulk, there are only two rates $\nu_{OT}$ and $\nu_{TO}$, while the dislocation produces a range of rates. As temperature increases, the relative size of these gaps decreases. The trend of $\Gamma_{\text{log},[3.4,100]}$ is well described by the CE model for all temperatures in Fig. 3.4(a). Even though $\Gamma_{\text{log},[3.4,100]}$ is a poor representation of $S_{\text{inc}}(Q,\omega)$, we find good agreement between $\Gamma_{\text{log},[3.4,100]}$ and the experimental widths in Fig. 3.4(b) by using the same fitting approach. As with experiment, we can extract a mean residence time and an average jump distance for each temperature from these fits to the Chudley-Elliott model, and make a model of diffusivity that we can compare with the direct KMC diffusivity values.

Fig. 3.5 shows that the jump distances extracted from the CE fits to $\Gamma_{\text{log},[3.4,100]}$ are nonmonotonic as a function of temperature and larger than distances in our dislocation geometry at higher temperatures, similar to those found by experiment. Jump distances between nearest neighbor octahedrals in the expanded region below the core, $\sim 2.74$Å, are less than 1% larger than the nearest neighbor octahedral distance in bulk. In the core, the interstitial sites are sheared, and it is difficult to classify these sites as octahedral or tetrahedral sites. However, the jump distances between every other site are similar to the nearest neighbor octahedral site distances below the core. The distance between each site in the core alternates between $\sim 1.43$Å and $\sim 1.62$Å. Distances between sites in

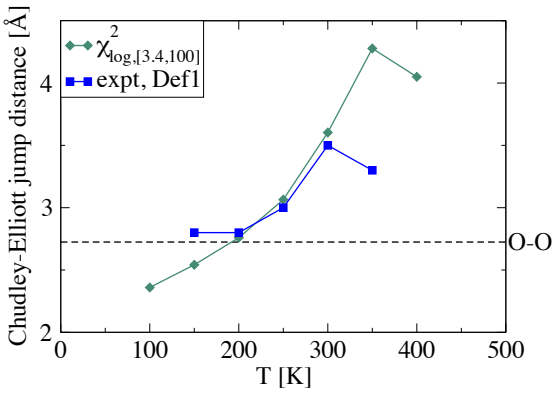


Figure 3.5: Jump distance as a function of temperature. The computed jump distances from CE fits to $\Gamma_{\log,[3.4,100]}$ vary nonmonotonically and span the same range as found in experiment.[71] For comparison, the distance between two octahedral sites in bulk $\approx 2.724$Å, and the distance between an octahedral site and a tetrahedral site $\approx 1.668$Å.

the core that connect to sites in the expanded region below the core are either $\sim 0.95$Å or $\sim 1.59$Å. None of these distances account for the large jump distances extracted from the CE model and $\chi^2_{\log,[3.4,100]}$. Rather, these distances suggest the behavior is an artifact of the fitting procedure.

Fig. 3.6 shows that the experiment-like fit $\chi^2_{\log,[3.4,100]}$ yields a diffusion barrier that is lower than the KMC diffusion barrier. From our KMC simulations we find an effective diffusion barrier of $E_a = 0.125$ eV. The diffusion barrier obtained from a CE fit to $\Gamma_{\log,[3.4,100]}$ is $E_a = 0.068$ eV, which matches the experimentally observed diffusion barrier.[71] Depending on temperature, different Lorentzian terms dominate $S_{\text{inc}}(Q,\omega)$ in the fixed range of $[3.4, 100]$. The lower diffusion barrier is a result of the $\chi^2_{\log,[3.4,100]}$ fit overpredicting diffusivity at low temperatures and underpredicting diffusivity at high temperatures. One might think that increasing the range of energies over which we fit $S_{\text{inc}}(Q,\omega)$ would improve the accuracy of the extracted diffusivity. However, we find that including lower energies in the fitting range $[1, 100]$ has little effect on the diffusivity. As we extend the experimental window from 100 $\mu$eV to 1600 $\mu$eV ($\chi^2_{\log,[3.4,1600]}$ to $\chi^2_{\log,[3.4,1600]}$), the extracted diffusivity approaches the diffusivity from $\bar{\lambda}$, which does not agree with the diffusivity from KMC simulations. We also compare these values to a linear least squares fit over the range of experimentally accessible energies, which is more sensitive to changes in the lower limit of the energy range.

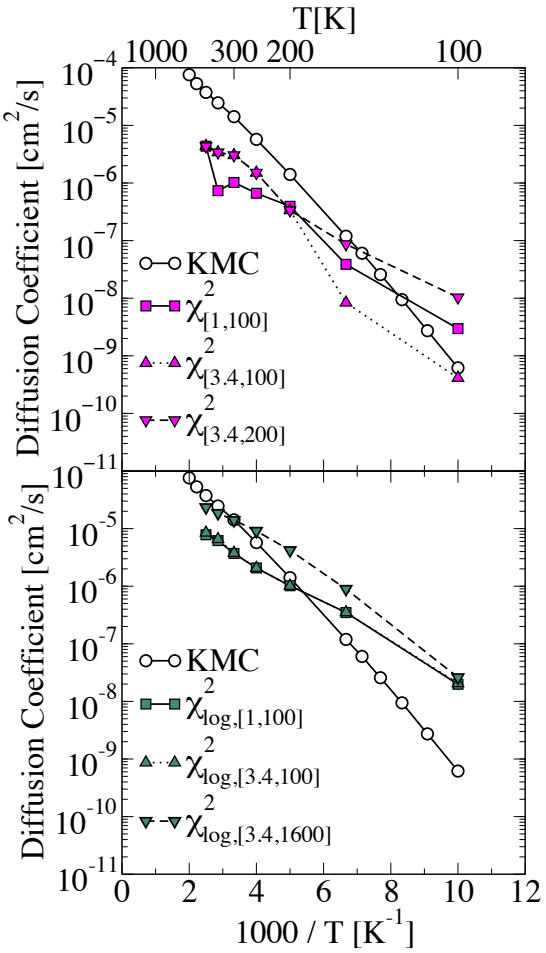


Figure 3.6: Diffusivities extracted from CE fits compared to diffusivity extracted from kinetic Monte Carlo simulations. The error bars of the KMC data points are smaller than the symbol sizes. A linear least squares fit over experimentally accessible energies $\chi^2_{[3.4,100]}$ underpredicts diffusivity and is noisy due to widths as a function of $Q$ that are not well described by the CE model. Increasing the experimental window $\chi^2_{[3.4,200]}$ and decreasing the experimental resolution $\chi^2_{[1,100]}$ predict slightly different diffusivities, but neither leads to better agreement with KMC. The diffusion barrier from the experiment-like fit $\chi^2_{\log,[3.4,100]}$ is smaller than the diffusion barrier from KMC simulations because $\chi^2_{\log,[3.4,100]}$ overpredicts diffusivity at low temperature but underpredicts diffusivity at high temperature. A smaller experimental resolution $\chi^2_{\log,[1,100]}$ has no effect on the extracted diffusivity. A larger experimental window $\chi^2_{\log,[3.4,1600]}$ predicts slightly different diffusivity but still does not improve agreement with the diffusivity obtained from KMC.

Using this linear least squares fit, the widths as a function of $Q$ are not well described by the CE model for any range of energies, especially for high temperatures, which leads to poor predictions of diffusivity.

## 3.4 Conclusion

This work illustrates two major conclusions. First, DFT is able to quantitatively predict pipe diffusion and is consistent with experiment. We find low diffusion barriers from sites in the expanded region below the partial core into the partial core and a novel diffusion pathway inside the partial core with low diffusion barriers. This pathway allows diffusing hydrogen atoms to bypass other hydrogen atoms by moving from the lowest energy states below the partials core to slightly higher energy states inside the partial cores. Second, traditional analysis of QENS spectra, i.e. representing $S_{\text{inc}}(Q,\omega)$ as a single Lorentzian and using a Chudley-Elliott model to extract diffusivities, oversimplifies the data and leads to errors in the diffusivity. Furthermore, these errors are difficult to detect using experimental data alone. The Chudley-Elliott model matches the trend of the experimental widths as a function of $Q$ and leads to an Arrhenius relationship between the model diffusivity and temperature. Only the jump distance as a function of temperature behaves unusually. Fixing the jump distance to be the bulk distance between nearest neighbor octahedral sites produces worse fits of the experimental widths as a function of $Q$ but has little effect on the model diffusivity. The deviation between the diffusivity we calculate with KMC and those we calculate using an experiment-like fit differs by more than what could be accounted for by differences between the fitted jump distances from experiment and bulk jump distances. Experiments need to be compared to the incoherent scattering function directly using a computational model that can predict the incoherent scattering function and diffusivity. This approach is general and could be applied to other systems with anisotropic diffusion, such as diffusion near grain boundaries and interfaces.

# CHAPTER 4

# INTERMEDIATE SCATTERING

## 4.1 Introduction

A variety of models have been proposed that attempt to extract physically meaningful quantities from QENS data for anisotropic diffusion systems[78, 139, 140]. The analysis of diffusion in isotropic and cubic systems has been established[73]. Analysis of QENS data was used to determine that hydrogen diffuses between octahedral sites in polycrystalline $\alpha$-palladium[86, 137] and in single crystal palladium[93]. Quasielastic neutron scattering data from hydrogen diffusion in palladium hydride and in palladium nanocrystals was fit with a sum of two Lorentzians and analyzed using the isotropic diffusion model[141]. However, the use of a model derived for isotropic diffusion is not necessarily appropriate for analyzing diffusion in an anisotropic system[142]. A model for analyzing one-dimensional diffusion has been developed by spherical averaging of the scattering function for diffusion of molecules in a one-dimensional channel[143–145]. The stretched exponential function, or its Fourier transform, is sometimes used to fit scattering data from anisotropic systems; however, the interpretation of the function's parameters is unclear[99, 146].

In this chapter, we compute the intermediate scattering function from *ab initio* data and compare our results with the combined the experimental data from two different instruments that cover different energy ranges. In Sect. 4.2, we calculate the intermediate scattering function. We analyze the results and compare with experiment in Sect. 4.3 and provide conclusions in Sect. 4.4. We find that our model is inadequate to capture the behavior of the intermediate scattering function at small times, which is likely due to contributions from vibrations of the hydrogen and the palladium

atoms to the experimental data.

## 4.2 Calculating the intermediate scattering function

Incoherent QENS experiments measure the double differential cross section[75], which for hydrogen is dominated by incoherent scattering[79]. In bulk palladium, the hydrogen atom diffuses from a ground state octahedral interstitial site through a tetrahedral interstitial site into a neighboring octahedral site to achieve long range diffusion[38]. The diffusion barrier from an octahedral site into a tetrahedral site, $E_{\mathrm{OT}} = 0.277$ eV, is much larger than the diffusion barrier from a tetrahedral site into an octahedral site, $E_{\mathrm{TO}} = 0.125$ eV. Diffusion experiments only measure the larger, rate-limiting barrier[123]. The incoherent scattering function $S_{\mathrm{inc}}(\mathbf{Q}, \omega)$ can be modeled as a sum of Lorentzians whose widths depend on the rates to diffuse between sites[78]. There are only two different diffusion barriers, i.e. two diffusion rates, in bulk, and one of those barriers is larger. Thus in the case of hydrogen diffusion in bulk, the incoherent scattering function, even when spherically averaged, can be approximated by a single Lorentzian[86]. The broken symmetry near a dislocation leads to a distribution of diffusion barriers[142]. Attempts to approximate the incoherent scattering function for hydrogen diffusion near an edge dislocation as a single Lorentzian and use the Chudley-Elliott model[73] to fit the widths of the Lorentzians as a function of $Q$ lead to errors in the diffusivity and unusual jump distances.

As an alternative to the incoherent scattering function, we can compute the self-part of the intermediate scattering function

$$I_{\mathrm{s}}(\mathbf{Q}, t) = \langle \exp\Big(i\mathbf{Q} \cdot (\mathbf{r}(t) - \mathbf{r}(t_0))\Big)\rangle, \tag{4.1}$$

which is related to self-diffusion and is analogous to the incoherent scattering function as a part of the total scattering function[75, 78]. Quasielastic neutron scattering data is a convolution of the $S_{\mathrm{inc}}(\mathbf{Q}, \omega)$ and the resolution function of the spectrometer[78]. Fourier transforming QENS

data results in a product of $I_s(\mathbf{Q}, t)$ and the resolution function, which makes the resolution function easier to separate from $I_s(\mathbf{Q}, t)$. This makes it is possible to compare $I_s(\mathbf{Q}, t)$ from different instruments. Using this approach, Arrighi *et al.* combined three sets of seemingly conflicting QENS data with different resolutions to find excellent overlap of data in the time domain[147]. As in our previous study[142], we assume the vibrational and diffusive motions are independent and only consider the diffusive term. This assumption is reasonable as long as the time scales of the vibrational and diffusive motions are well separated[148], which is the case for hydrogen in palladium[123]. In general, the contribution from vibrations can be approximated as changes to the intensity of the measured spectra[75]. Using a similar jump matrix analysis[78] as our previous work[142] for calculating the incoherent scattering function, the diffusive self-part of the intermediate scattering function can be expressed as a sum of exponentials

$$I_s^d(\mathbf{Q}, t) = \sum_{i=1}^{N_{\text{sites}}} w_i(\mathbf{Q}) e^{\lambda_i(\mathbf{Q})t}, \tag{4.2}$$

where $w_i(\mathbf{Q})$ and $\lambda_i(\mathbf{Q})$ are the weights and widths computed from the jump matrix. We spherically average $I_s^d(\mathbf{Q}, t)$ over a grid of $\mathbf{Q}$-points in the same manner that we spherically averaged $S_{\text{inc}}(\mathbf{Q}, \omega)$ in our previous study. Combining experimental data from multiple instruments with different resolutions produces data over a wider range of $t$, with which we can test our model.

## 4.3 Analyzing the intermediate scattering function

Just as $S_{\text{inc}}(\mathbf{Q}, \omega)$ from hydrogen in a dislocation cannot be approximated by a single Lorentzian, $I_s^d(Q, t)$ from anisotropic hydrogen diffusion cannot be described by a single decaying exponential function. We fit $I_s^d(Q, t)$ with the Kohlraush-Williams-Watts model[99], Eqn. (1.11). Measurements from a variety of systems exhibit behavior that follow the KWW model[101–105], and for some of these systems, the KWW model can be derived from physical mechanisms. Klafter and Shlesinger derived the KWW model for relaxation through direct transfer to nearest neighbor

defects, relaxation through hierarchically constrained levels, and relaxations triggered by defect diffusion[149]. The ability to map these systems onto the same model is due to the scale-invariant relaxation rates in each system.

Fig. 4.1 shows that the KWW model describes the behavior of the experimentally measured $I_s(Q,t)$ and simulated $I_s^d(Q,t)$ well. Discrete Fourier transforms of the original data allow us to combine the data collected from two different instruments: the time-of-flight neutron backscattering silicon spectrometer[150] (BASIS) and the cold neutron chopper spectrometer[151] (CNCS) at the Spallation Neutron Source in Oak Ridge National Lab. We used only the BASIS data in our previous study[142]. Deviations between the experimental data and the KWW model become noticeable as temperature increases for larger $Q$-values. The simulated data deviates from the KWW model at small times.

Fig. 4.2 shows good agreement between the $\tau$-values extracted from our simulations and the experimental data but larger $\beta$-values from the simulations than from the experimental data. The range of time covered by experiment is about [1, 1000] ps, which corresponds to an energy range of about [4 $\mu$eV,4 meV]. For our simulations, we only consider the diffusive motion of the hydrogen atom. However, the smallest times (or largest energies) of the experimental range approach the inelastic range[86, 98], which may be responsible for the disagreement between $\beta$-values from our simulations and those extracted from the experimental data.

Fig. 4.3 compares the rate-scaled simulated $I_s^d(Q,t)$ to $I_s(Q,t)$ from experiment. The diffusion barrier in bulk from experiment is 0.230 eV[123], while the diffusion barrier from ab initio simulations is 0.277eV[142]. Differences between the experimental rates and our ab initio rates would be a reasonable expectation. We multiply the rates in our model by a constant factor and find the value of this constant that minimizes the least squares error between our model and the experimental data. This factor is less than one for all temperatures, which suggests that the rates in our simulations of hydrogen in the dislocation geometry are faster than rates measured by the QENS experiments for hydrogen in a deformed sample. The shape of the simulated $I_s^d(Q,t)$ differs from the trend of the experimental data, and these deviations become more apparent at shorter times,

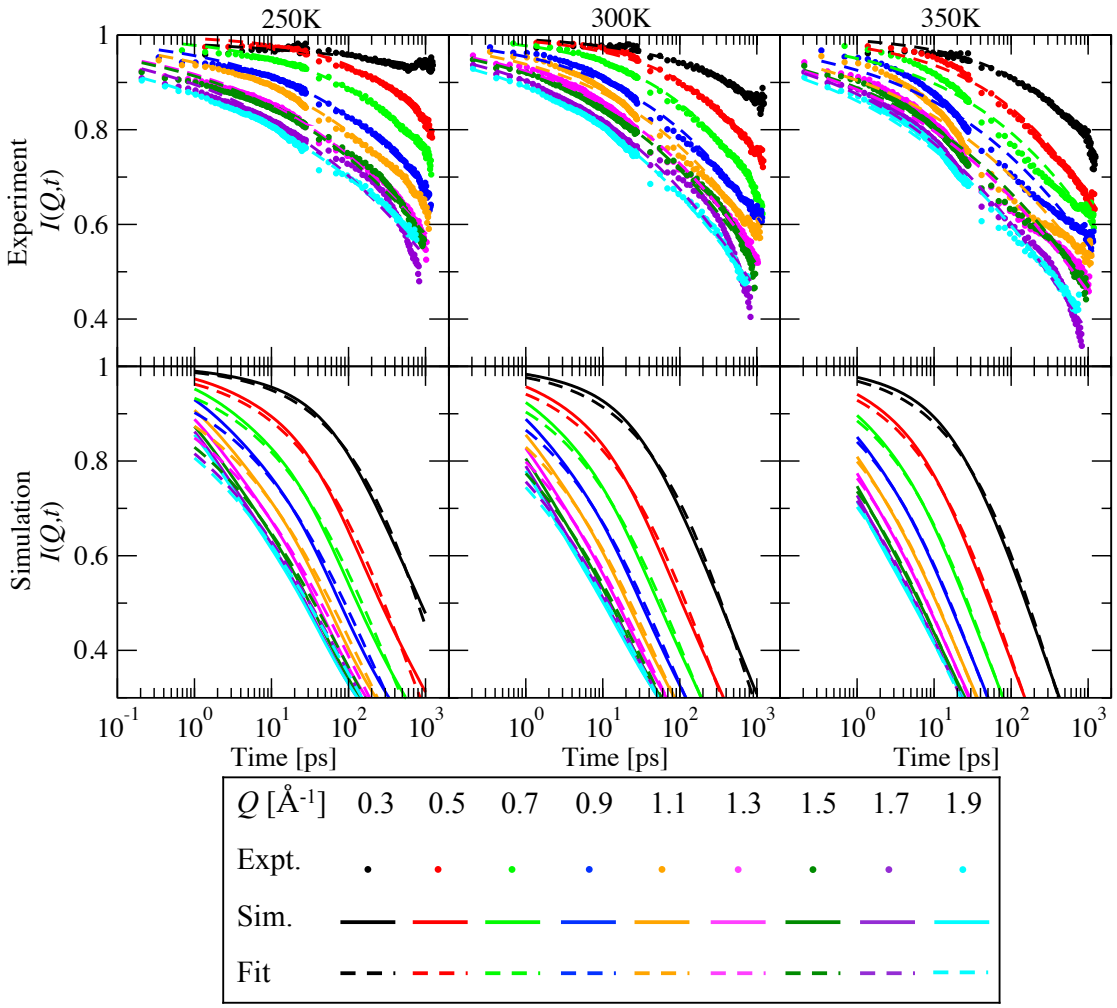


Figure 4.1: Linear least squares fits of KWW model to experimental $I_s(Q,t)$ and simulated $I_s^d(Q,t)$ over a time range of $[1, 1000]$ ps. The fits (dashed) represent $I_s(Q,t)$ well for 250K and 300K, but the experimental data at 350K deviates from the fit. The simulated data for each temperature and $Q$-value decays faster than the experimental data when evaluated over the same time range as experiment.

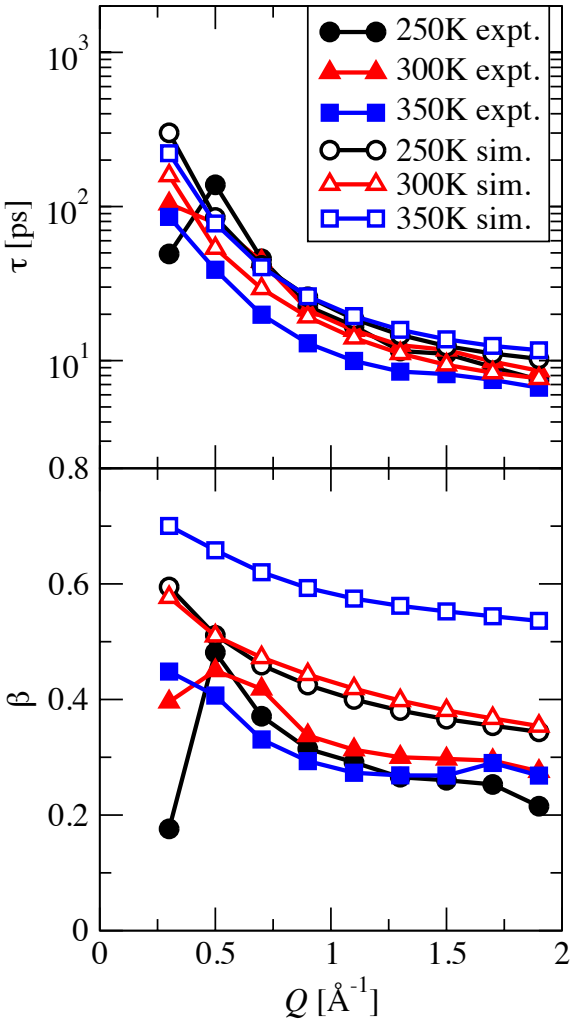


Figure 4.2: Parameters extracted from linear least squares fits of the KWW model to the experimental $I_s(Q,t)$ and the simulated $I_s^d(Q,t)$ over a time range of $[1, 1000]$ ps. The $\tau$-values from the simulated data and the experimental data agree well. The $\beta$-values for the simulation data over $[1, 1000]$ ps are larger than the $\beta$-values extracted from the experimental data and show temperature dependence unlike the parameters from the experimental data.

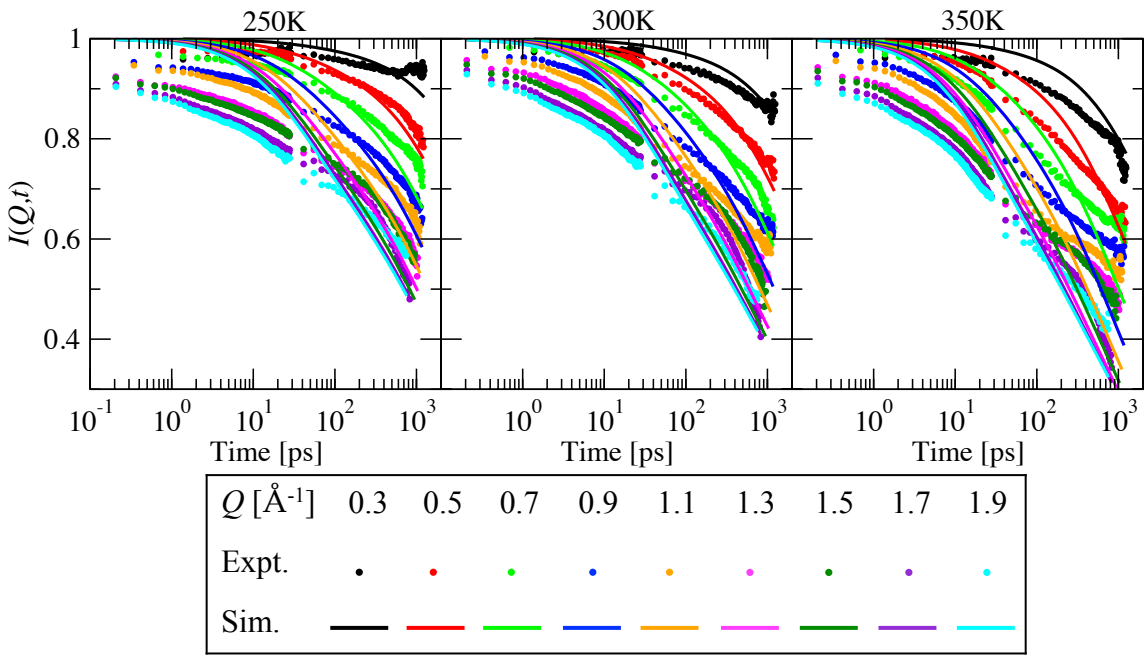


Figure 4.3: Experimental $I_s(Q,t)$ compared to rate-scaled simulated $I_s^d(Q,t)$. The rates for our simulation are scaled by a constant factor in order to compare the trend of the experimental data with the shape of our calculated $I_s^d(Q,t)$. These scaling factors are 0.038, 0.026, and 0.026 at 250K, 300K, and 350K. The simulated data deviates from the experimental data at small $t$.

i.e. higher energies.

## 4.4 Conclusion

Our model does not capture the behavior of the intermediate scattering function at small times. We neglect the vibrations of the hydrogen, vibrations of the palladium atoms, and resonant vibrations[152, 153]. The vibrational motion of the hydrogen atom contributes to $S_{\text{inc}}(\mathbf{Q},\omega)$ in the form of a Debye-Waller factor as long the amplitude of the vibrational motion is small, and the vibration is decoupled from the diffusive motion[154]. However, the contribution of vibrations to the QENS data may be more complicated and incorporating the effects of vibrations will likely be challenging. A more accurate model of the total incoherent scattering function or the self-part of the intermediate scattering function incorporating both diffusion and vibration motion may necessitate molecular dynamics simulations[78]. The vibrations of the hydrogen atom as well as the

vibration of the palladium atoms and the influence of the host atom vibrations on the diffusing hydrogen may have significant effects[155]. In addition, the quantum nature of the hydrogen nucleus may contribute to the incoherent scattering, so a complete model may also require the inclusion of hydrogen tunneling, which becomes increasingly important at low temperatures. Kyriakou *et al.* showed that the quantum crossover temperature hydrogen near a Pd/Cu surface is 260K. We see deviations approximately at or above this crossover temperature. Therefore, we conclude that the deviation in our model at small times is not due to the quantum mechanical behavior of the hydrogen nucleus.

# CHAPTER 5

# CONCLUSION

## 5.1 Summary of Results

Density functional theory calculates sites energies on the tensile side of the slip plane of an $\frac{a}{2}[110](1\bar{1}\bar{1})$ edge dislocation in palladium and in the dislocation core that are lower than the site energy of an octahedral site in bulk palladium. We find diffusion barriers in the expanded region below the core that are smaller than the diffusion barriers in bulk and even lower barriers along the minimum energy pathway inside the dislocation core. In addition, the calculated diffusion barriers from the expanded sites into the partials cores are small compared to the diffusion barriers in bulk. Thus, we predict that accelerated diffusion along the threading direction occurs by hydrogen atoms binding to the attractive sites near the dislocation, diffusing into the dislocation core, and traveling along the the dislocation core. This proposed mechanism allows diffusing hydrogen atoms to bypass other hydrogen atoms and avoid being slowed down due to a hydrogen-hydrogen blocking interaction.

Kinetic Monte Carlo simulations predict pipe diffusion of hydrogen near an edge dislocation. From our simulations, we find that the hydrogen atom diffuses farther along the threading direction than along directions perpendicular to the threading direction over the same amount of time. We also see the trapping of hydrogen to the dislocation core. At lower temperatures the hydrogen atom does not attempt to jump outside the bounds of the dislocation geometry supercell. The diffusion barrier extracted from an Arrhenius fit to our KMC simulations of hydrogen diffusion near a dislocation is smaller than the barrier to diffuse in the expanded region below the dislocation core and agrees with the barrier of the minimum energy pathway inside the dislocation core.

The common fitting procedure for experimental QENS data is not reliable for diffusion in anisotropic systems. We fit a single Lorentzian to the incoherent scattering function data and use the Chudley-Elliott model for isotropic diffusion to analyze the widths of these Lorentzians as a function of the scattering wavenumber $Q$. We find that this fitting procedure leads to an underestimation of the diffusion barrier by underpredicting diffusivities at high temperatures and overpredicting diffusivities at low temperatures. In addition, this fitting procedure yields unusual jump distances that are not based on physical jump distances in the geometry.

Our model fails to accurately describe the behavior of the intermediate scattering function at small times. Fourier transforming the experimental QENS data allows us to combine data from different instruments and to directly compare with our simulated intermediate scattering function. For both experiment and simulation, we find that a stretched exponential can fit the trend of the intermediate scattering function from hydrogen diffusion near a dislocation. Unfortunately, there is some disagreement at small times between the calculated function and the experimental data, which is highlighted by differences in the shape parameter $\beta$ for our simulations compared to experiment. These differences are likely due to vibrations in the real system that we do not take into account for our simulations.

## 5.2 Limitations and Future Work

We assume that the hydrogen nucleus diffuses classically and model the hydrogen atom jumps as instantaneous. We approximate site energies and energy barriers away from the stacking fault and partial dislocation cores by taking advantage of the fact that these energies vary linearly with respect to strain. This approximation leads to small errors in the energies of less than 25 meV. We use a constant prefactor of $10^{13} s^{-1}$. Improving upon this approximation would require calculating the vibrational modes at the ground state and the transition state. We do not account for the effect of vibrations in our calculation of the incoherent and intermediate scattering functions. Our model assumes that the vibrational and diffusional motion of the hydrogen atom are independent.

A more accurate model could use molecular dynamics to study the effect of vibrations. Quantum effects become more important at lower temperatures. Future work could use path integral molecular dynamics to incorporate hydrogen tunneling. *Ab initio* molecular dynamics simulations that accounted for the quantum behavior of the hydrogen nucleus would be computationally unreasonable. Future steps to incorporate the vibrational motion of the palladium and hydrogen atoms as well as the tunneling behavior of the hydrogen atom will likely require a classical potential.

We only consider a single hydrogen atom in an edge dislocation, which precludes the study of finite concentration effects. Our model cannot account for correlated jumps of the hydrogen, the formation of hydrides, or any type of interaction between hydrogen atoms. Anderson *et al.* studied finite concentrations $c$ of hydrogen in bulk palladium and found that the primary contribution to changes in the incoherent scattering function is the blocking interaction that prevents two hydrogen atoms from occupying the same site[156]. These authors calculated the widths using the Chudley-Elliott model and a mean residence time that was scaled by $1/(1-c)$ and a correlation factor that also depends on concentration. The changes due to finite concentrations of hydrogen were significant for a similar temperature range as was used in the experiments by Heuser *et al.*[71] and the temperature range considered in this work, but only for high concentrations of hydrogen. Furthermore, our simulations only include information for a single edge dislocation pointed along $[1\bar{1}2]$. We chose to study an edge dislocation because screw dislocations do not volumetrically strain the lattice. This choice is reasonable considering that hydrogen interstitial atoms bind to volumetrically expanded sites near an edge dislocation and we would not expect as strong of an attraction between a hydrogen atom and a screw dislocation. For the scattering analysis, we spherically average the scattering functions in order to compare with experimental data from polycrystalline palladium. The supercell that we use for the edge dislocation is periodic along the threading direction with fixed boundary conditions along directions perpendicular to the threading direction. When a hydrogen atom in our KMC simulations jumps to a site of the dislocation geometry with no connections leading further away from the dislocation core, we consider it to have escaped with no chance of jumping back into the simulation supercell. We do not consider con-

nections that lead out of the dislocation supercell when creating the jump matrix, which informs calculation of both the incoherent scattering function and the self-part of the intermediate scattering function. Our treatment of the supercell boundary perpendicular to the threading direction is simplifies the real system. In a real system, the dislocation would be surrounded by additional palladium atoms arranged either as bulk or according to the strain field of neighboring dislocations or grain boundaries. A future study could couple the edge dislocation geometry to bulk.

# REFERENCES


[1] J. Towns, T. Cockerill, M. Dahan, I. Foster, K. Gaither, A. Grimshaw, V. Hazlewood, S. Lathrop, D. Lifka, G. Peterson, R. Roskies, J. Scott, and N. Wilkins-Diehr, XSEDE: Accelerating Scientific Discovery, Computing in Science Engineering **16**(5), 62–74 (Sept 2014).

[2] C. A. Zapffe and C. E. Sims, Hydrogen embrittlement, internal stress and defects in steel, Transactions of the American Institute of Mining, Metallurgical and Petroleum Engineers **145**, 225–271 (1941).

[3] M. R. Louthan, G. R. Caskey, J. A. Donovan, and D. E. Rawl, Hydrogen embrittlement of metals, Materials Science and Engineering **10**, 357–368 (January 1972).

[4] D. S. Shih, I. M. Robertson, and H. K. Birnbaum., Hydrogen embrittlement of titanium: in situ TEM studies, Acta Metallurgica **36**(1), 111–1224 (January 1988).

[5] R. A. Oriani, A mechanistic theory of hydrogen embrittlement of steels, Berichte der Bunsengesellschaft für physikalische Chemie **76**(8), 848–857 (August 1972).

[6] C. T. Liu, E. H. Lee, and C. G. McKamey, An environmental effect as the major cause for room-temperature embrittlement in FeAl, Scripta metallurgica **23**(6), 875–880 (June 1989).

[7] J. P. Hirth, Effects of hydrogen on the properties of iron and steel, Metallurgical Transactions **11**(6), 861–890 (June 1980).

[8] M. R. Louthan, Hydrogen embrittlement of metals: a primer for the failure analyst, Journal of Failure Analysis and Prevention **8**(3), 289–307 (June 2008).

[9] S. Brahimi, R. Aguilar, and C. Christensen, Metallurgical analysis of Bay Bridge broken anchor rods S1-G1 & S2-A6, Technical report, Anamet, Inc., May 2013.

[10] G. F. V. Voort, Embrittlement of steels, in *ASM Handbooks Online*, volume 1, Properties and Selection: Irons, Steels, and High-Performance Alloys, pages 689–736, ASM International, 1990.

[11] P. S. Pao, Mechanisms of Corrosion Fatigue, in *ASM Handbooks Online*, volume 19, Fatigue and Fracture, pages 185–192, ASM International, 1996.

[12] A. Gurlo and D. Clarke, High-sensitivity hydrogen detection: Hydrogen-induced swelling of multiple cracked palladium films on compliant substrates, Angewandte Chemie International Edition **50**(43), 10130–10132 (2011).

[13] K. Nasako, Y. Ito, N. Hiro, and M. Osumi, Stress on a reaction vessel by the swelling of a hydrogen absorbing alloy, Journal of Alloys and Compounds **264**, 271–276 (1998).

[14] P. D. Khinskii and V. P. Krylov, The development of fisheyes in the fractures of steel samples, Metal Science and Heat Treatoment **12**(7), 618–621 (July 1970).

[15] P. G. Shewmon, Hydrogen attack of carbon steel, Metallurgical Transactions **7**(2), 279–286 (February 1976).

[16] J. R. Thygeson and M. C. Molstad, High pressure hydrogen attack of steel, Journal of Chemical and Engineering Data **9**(2), 309–315 (April 1964).

[17] M. Ransick and P. Shewmon, Effect of cold work on hydrogen attack, Metallurgical Transactions A **12A**, 17–22 (1981).

[18] C. Treischel, The cause and control of "blistering" in sheet-steel enameling, Journal of the American Ceramic Society **2**(10), 774–781 (October 1919).

[19] X. C. Ren, G. B. Shan, W. Y. Chu, J. X. Li, Y. J. Su, and L. J. Qiao, A Nucleation Mechanism of Hydrogen Blister in Metals and Alloys, Metallurgical and Materials Transactions A **39A**, 87–97 (January 2008).

[20] H. K. Birnbaum and P. Sofronis, Hydrogen-enhanced localized plasticity—a mechanism for hydrogen-related fracture, Materials Science and Engineering: A **176**(1-2), 191–202 (March 1994).

[21] I. M. Robertson, The effect of hydrogen on dislocation dynamics, Engineering Fracture Mechanics **68**(6), 671–692 (April 2001).

[22] J. A. Donovan, Sorption of tritium by nickel during plastic deformation, Metallurgical Transactions A **7A**, 145–149 (January 1976).

[23] M. Kurkela and R. Latanision, The effect of plastic deformation on the transport of hydrogen in nickel, Scripta metallurgica **13**(10), 927–932 (1979).

[24] N. Z. Muradov and T. N. Veziroğlu, From hydrocarbon to hydrogen–carbon to hydrogen economy, International Journal of Hydrogen Energy **30**(3), 225–237 (March 2005).

[25] R. E. Buxbaum and A. B. Kinney, Hydrogen transport through tubular membranes of palladium-coated tantalum and niobium, Industrial & Engineering Chemistry Research **35**(2), 530–537 (February 1996).

[26] U. Bossel, Does a hydrogen economy make sense?, Proceedings of the IEEE **94**(10), 1826–1837 (October 2006).

[27] B. Sakintuna, F. Lamari-Darkrim, and M. Hirscher, Metal hydride materials for solid hydrogen storage: a review, International Journal of Hydrogen Energy **32**(9), 1121–1140 (June 2007).

[28] L. Schlapbach and A. Züttel, Hydrogen-storage materials for mobile applications, Nature **414**, 353–358 (November 2001).

[29] H. Wagner and H. Horner, Elastic interaction and the phase transition in coherent metal-hydrogen systems, Advances in Physics **23**(4), 587 (1974).

[30] V. M. Skripnyuk, E. Rabkin, Y. Estrin, and R. Lapovok, Improving hydrogen storage properties of magnesium based alloys by equal channel angular pressing, International Journal of Hydrogen Energy **34**(15), 6320–6324 (August 2009).

[31] D. K. Ross, Hydrogen storage: the major technological barrier to the development of hydrogen fuel cell cars, Vacuum **80**(10), 1084–1089 (August 2006).

[32] K. Edalati, J. Matsuda, M. Arita, T. Daio, E. Akiba, and Z. Horita, Mechanism of activation of TiFe intermetallics for hydrogen storage by severe plastic deformation using high-pressure torsion, Applied Physics Letters **103**(14), 143902 (September 2013).

[33] T. B. Flanagan, J. F. Lynch, J. D. Clewley, and B. V. Turkovich, The effect of lattice defects on hydrogen solubility in palladium: I. Experimentally observed solubility enhancements and thermodynamics of absorption, Journal of Less Common Metals **49**, 13–24 (September 1976).

[34] J. A. Rayne, Elastic Constants of Palladium from 4.2–300K, Physical Review **118**(6), 1545 (June 1960).

[35] J. Shu, B. P. A. Grandjean, A. V. Neste, and S. Kaliaguine, Catalytic palladiumbased membrane reactors: A review, The Canadian Journal of Chemical Engineering **69**(5), 1036–1060 (October 1991).

[36] S. Wilke, D. Hennig, and R. Löber, Ab initio calculations of hydrogen adsorption on (100) surfaces of palladium and rhodium, Physical Review B **50**(4), 2548 (July 1994).

[37] T. Mitsui, M. K. Rose, E. Fomin, D. F. Ogletree, and M. Salmeron, Dissociative hydrogen adsorption on palladium requires aggregates of three or more vacancies, Nature **422**(6933), 705–707 (April 2003).

[38] Y. M. Koroteev, O. Gimranova, and I. Chernov, Hydrogen migration in palladium: First-principles calculations, Physics of the Solid State **53**(5), 896–900 (October 2011).

[39] L. L. Jewell and B. H. Davis, Review of absorption and adsorption in the hydrogen–palladium system, Applied Cataysis A: General **310**, 1–15 (2006).

[40] F. D. Manchester, A. San-Martin, and J. M. Pitre, The H-Pd (hydrogen-palladium) system, Journal of Phase Equilibria **15**(1), 62–83 (February 1994).

[41] A. G. Knapton, Palladium alloys for hydrogen diffusion membranes, Platinum Metals Review **21**(2), 44–50 (April 1977).

[42] Y. Cao, H. L. Li, J. A. Szpunar, and W. Shmayda, Modeling of hydrogen trapping in the deformed Pd and Pd 77 Ag 23 alloy, Materials Science and Engineering: A **379**(1), 173–180 (August 2004).

[43] J. A. Rodrigues and R. Kirchheim, More evidence for the formation of a dense cottrell cloud of hydrogen (hydride) at dislocations in niobium and palladium, Scripta metallurgica **17**(2), 159–64 (February 1983).

[44] M. Maxelon, A. Pundt, W. Pyckhout-Hintzen, J. Barker, and R. Kirchheim, Interaction of hydrogen and deuterium with dislocations in palladium as observed by small angle neutron scattering, Acta materialia **49**(14), 2625–2634 (August 2001).

[45] D. R. Trinkle, H. Ju, B. J. Heuser, and T. J. Udovic, Nanoscale hydride formation at dislocations in palladium: Ab initio theory and inelastic neutron scattering measurements, Physical Review B **83**(17), 174116 (May 2011).

[46] R. Heller and H. Wipf, Diffusion coefficient, heat of transport, and solubility limit of H in V, Phys. Stat. Sol. (a) **33**(2), 525–529 (February 1976).

[47] H. Ogawa, Atomistic simulation of hydrogen dynamics near dislocations in vanadium hydride, ournal of Alloys and Compounds **645**, S205–S208 (October 2015).

[48] R. Kirchheim, Interaction of hydrogen with dislocations in palladium—I. Activity and diffusivity and their phenomenological interpretation, Acta Metallurgica **29**(5), 835–843 (May 1981).

[49] D. Turnbull and R. E. Hoffman, The effect of relative crystal and boundary orientations on grain boundary diffusion rates, Acta Metallurgica **2**(3), 419–26 (May 1954).

[50] E. W. Hart, On the role of dislocations in bulk diffusion, Acta Metallurgica **5**(10), 597 (October 1957).

[51] G. R. Love, Dislocation Pipe Diffusion, Acta Metallurgica **12**(6), 731–737 (June 1964).

[52] R. W. Balluffi, On measurements of selfdiffusion rates along dislocations in FCC Metals, Physica Status Solidi **42**(1), 11–34 (January 1970).

[53] K. T. Aust and B. Chalmers, Surface energy and structure of crystal boundaries in metals, Proceedings of the Royal Society of London A: Mathematical, Physical and Engineering Sciences **204**(1078), 359–366 (December 1950).

[54] R. E. Hoffman and D. Turnbull, Lattice and grain boundary self-diffusion in silver, Journal of Applied Physics **22**(5), 634–639 (May 1951).

[55] G. Love and P. G. Shewmon, Self-diffusivity of silver in twist boundaries, Acta Metallurgica **11**(8), 899–906 (August 1963).

[56] M. Wuttig and H. K. Birnbaum, Self-diffusion along edge dislocations in nickel, Physical Review **147**(2), 495 (1966).

[57] T. E. Volin and R. W. Balluffi, Direct observation of rapid self-diffusion along dislocations in aluminum, Applied Physics Letters **11**(8), 259–261 (October 1967).

[58] T. E. Volin and R. W. Balluffi, Annealing kinetics of voids and the self-diffusion coefficient in aluminum, Physica Status Solidi **25**(1), 163–173 (January 1968).

[59] T. E. Volin, K. H. Lie, and R. W. Balluffi, Measurement of rapid mass transport along individual dislocation in aluminum, Acta Metallurgica **19**(4), 263–274 (April 1971).

[60] X. Tang, K. P. D. Lagerlöf, and A. H. Heuer, Determination of pipe diffusion coefficients in undoped and magnesia-doped sapphire ($\alpha$-Al2O3): A study based on annihilation of dislocation dipoles, Journal of the American Ceramic Society **86**(4), 1560–65 (April 2003).

[61] M. Legros, G. Dehm, E. Arzt, and T. J. Balk, Observation of giant diffusivity along dislocation cores, Science **319**(5870), 1646–1649 (March 2008).

[62] X. Zhang and G. Lu, Calculation of fast pipe diffusion along a dislocation stacking fault ribbon, Physical Review B **82**(1), 012101 (July 2010).

[63] H. Kimizuka and S. Ogata, Slow diffusion of hydrogen at a screw dislocation core in $\alpha$-iron, Physical Review B **84**(2), 024116 (2011).

[64] C. Baker, M. Wuttig, and H. K. Birnbaum, Diffusion along edge dislocations in Ni-Co alloys, Technical Report C00-1198-477, University of Illinois at Urbana-Champaign, August 1967.

[65] R. S. Barnes, The generation of vacancies in metals, Philosophical Magazine **5**(54), 635–646 (June 1960).

[66] J. Huang, M. Meyer, and V. Pontikis, Is pipe diffusion in detals vacancy controlled? A molecular-dynamics study of an edge dislocation in copper, Physical Review Letters **63**(6), 1516–1519 (August 1989).

[67] J. Huang, M. Meyer, and V. Pontikis., Core structure of a dissociated edge dislocation and pipe diffusion in copper investigated by molecular dynamics, Journal de Physique III **1**(6), 867–883 (June 1991).

[68] T. Nakagawa, A. Nakamura, I. Sakaguchi, N. Shibata, K. P. D. Lagerlöf, T. Yamamoto, J. Haneda, and Y. Ikuhara, Oxygen pipe diffusion in sapphire basal dislocation, Journal of the Ceramic Society of Japan **114**(11), 1013–1017 (July 2006).

[69] R. E. Pawel and T. S. Lundy, Diffusion of Nb95 into tantalum single crystals, Acta Metallurgica **13**(3), 345–351 (March 1965).

[70] J. Mimkes, Pipe diffusion along isolated dislocations, Thin Solid Films **25**(1), 221–230 (January 1975).

[71] B. J. Heuser, D. R. Trinkle, N. Jalarvo, J. Serio, E. J. Schiavone, E. Mamontov, and M. Tyagi, Direct measurement of hydrogen dislocation pipe diffusion in deformed Pd using quasielastic neutron scattering, Physical Review Letters **113**(2), 025504 (July 2014).

[72] J. V. Pezold, L. Lymperakis, and J. Neugebeauer, Hydrogen-enchanced localized plasticity at dilute bulk H concentrations: the role of H-H interactions and the formation of local hydrides, Acta Materialia **59**(8), 2969–2980 (2011).

[73] C. T. Chudley and R. J. Elliott, Neutron scattering from a liquid on a jump diffusion model, Proceedings of the Physical Society **77**(2), 353–361 (1961).

[74] T. Springer, Quasielastic neutron scattering for the investigation of diffusive motions in solids and liquids, Springer tracts in modern physics **64**, 1–100 (1972).

[75] J. Embs, F. Juranyi, and R. Hempelmann, Introduction to quasielastic neutron scattering, Zeitschrift für Physikalische Chemie **224**(1-2), 5–32 (2010).

[76] L. Liang, R. Rinaldi, and H. Schober, editors, *Neutron applications in earth, energy, and environmental sciences*, Springer US, 2009.

[77] L. V. Hove, Correlations in space and time and Born approximation scattering in systems of interacting particles, Physical Review **95**(1), 249 (July 1954).

[78] R. Hempelmann, *Quasielastic Neutron Scattering*, Oxford University Press, 2000.

[79] V. F. Sears, Neutron scattering lengths and cross sections VARLEY, Neutron News **3**(3), 26–37 (1992).

[80] D. J. Hughes, H. Palevsky, W. Kley, and E. Tunkelo, Atomic motions in water by scattering of cold neutrons, Physical Review **119**(3), 872 (August 1960).

[81] V. F. Sears, Cold neutron scattering by molecular liquids: III. Methane, Canadian Journal of Physics **45**(2), 237–254 (February 1967).

[82] B. A. Dasannacharya and G. Venkataraman, Dynamics of liquid $CH_4$ from cold-neutron scattering, Physical Review **156**(1), 196 (April 1967).

[83] G. H. Vineyard, Scattering of slow neutrons by a liquid, Physical Review **110**(5), 999 (June 1958).

[84] B. N. Brockhouse, Diffusive Motions in Liquids and Neutron Scattering, Physical Review Letters **2**(7), 287 (April 1959).

[85] D. J. Hughes, H. Palevsky, W. Kley, and E. Tunkelo, Atomic motions in water by scattering of cold neutrons, Physical Review Letters **3**(2), 92 (July 1959).

[86] K. Sköld and G. Nelin, Diffusion of hydrogen in the $\alpha$-phase of Pd-H studied by small energy transfer neutron scattering, J. Phys. Chem. Solids **28**, 1369–2380 (June 1967).

[87] I. Pelah, W. L. Whittemore, and A. W. McReynolds, Energy Distributions of Neutrons Scattered by Liquid Lead, Physical Review **113**(3), 767 (February 1959).

[88] B. N. Brockhouse and N. K. Pope, Time-dependent pair correlations in liquid lead, Physical Review Letters **3**(6), 259 (September 1959).

[89] J. M. Rowe, K. Sköld, H. E. Flotow, and J. J. Rush, Quasielastic Neutron Scattering by Hydrogen in the $\alpha$ and $\beta$ Phases of Vanadium Hydride, J. Phys. Chem. Solids **32**(1), 41–54 (1971).

[90] K. Funke, T. Kloidt, and D. Wilmer, Jump relaxation in $RbAg_4I_5$ by dynamic conductivity and quasielastic neutron scattering, Solid State Ionics **53**, 947–954 (July 1992).

[91] V. Lottner, U. Buchenau, and W. J. Fitzgerald, Incoherent structure factor of hydrogen in $NbH_0.11$, Zeitschrift für Physik B Condensed Matter **35**(1), 35–41 (March 1979).

[92] M. Björketun, P. Sundell, and G. Wahnström, A kinetic Monte Carlo study of proton diffusion in disordered perovskite structured lattices based on first-principles calculations, Solid State Ionics **176**(39-40), 3035–3040 (2005).

[93] J. M. Rowe, J. J. Rush, L. A. deGraaf, and G. A. Ferguson, Neutron Quasielastic Scattering Study of Hydrogen Diffusion in a Single Crystal of Palladium, Physical Review Letters **29**(18), 1250 (October 1972).

[94] D. Richter and T. Springer, Diffusion of hydrogen in niobium in the presence of trapping impurities studied by neutron spectroscopy, Physical Review B **18**(1), 126–140 (1978).

[95] J. W. M. Frenken, B. J. Hinch, J. P. Toennies, and C. Wöll, Anisotropic diffusion at a melting surface studied with He-atom scattering, Physical Review B **41**(2), 938–946 (1990).

[96] W. S. Howells, The use of Fourier transforms in the analysis of QENS data, Physica B **226**, 78–81 (1996).

[97] A. Arbe, J. Colmenero, and D. Gomez, Merging of the $\alpha$ and $\beta$ relaxations in polybutadiene: A neutron spin echo and dielectric study, Physical Review E **54**(4), 3853–3869 (1999).

[98] S. F. Parker and P. Collier, Applications of neutron scattering in catalysis, Johnson Matthey Technology Review **60**(2), 132–144 (April 2016).

[99] G. Williams and D. C. Watts, Non-symmetrical dielectric relaxation behaviour arising from a simple empirical decay function, Transactions of the Faraday Society **66**, 80–85 (1970).

[100] E. W. Montroll and J. T. Bendler, On Lévy (or stable) distributions and the Williams-Watts model of dielectric relaxation, Journal of Statistical Physics **34**(1-2), 129–162 (1984).

[101] G. Patterson, Photon Correlation Spectroscopy, Advances in Polymer Science **48**(1), 125–159 (1983).

[102] A. A. Jones, J. F. O'Gara, P. T. Inglefield, J. T. Bender, A. F. Yee, and K. L. Ngai, Proton spin relaxation and molecular motion in a bulk polycarbonate, Macromolecules **16**, 658–665 (1983).

[103] R. Chamberlin, G. Mozurkewich, and R. Orbach, Time decay of the remanent magnetization in spin-glasses, Physical Review Letters **52**(10), 867–870 (1984).

[104] D. LeGrand, W. Olszewski, and J. Bendler, Anelastic and plastic response of polymers, Annals of the New York Academy of Sciences **484**, 301–310 (1986).

[105] I. Svare, S. Martin, and F. Borsa, Stretched exponentials with T -dependent exponents from fixed distributions of energy barriers for relaxation times in fast-ion conductors, Physical Review B **61**(1), 228–233 (2000).

[106] H. D and D. J. Bacon, *Introduction to dislocations*, Elsevier Ltd., fourth edition edition, 2001.

[107] G. I. Taylor, The mechanism of plastic deformation of crystals. Part I. Theoretical, Proceedings of the Royal Society of London. Series A, Containing Papers of a Mathematical and Physical Character **145**(855), 362–387 (July 1934).

[108] E. Orowan, Plasticity of crystals, Zeitschrift für Physik **89**(9-10), 605–659 (1934).

[109] M. Polanyi, Lattice distortion which originates plastic flow, Zeitschrift für Physik **89**, 660–662 (1934).

[110] J. M. Hedges and J. W. Mitchell, The observation of polyhedral sub-structures in crystals of silver bromide, The London, Edinburgh, and Dublin Philosophical Magazine and Journal of Science **44**(349), 223–224 (February 1953).

[111] F. C. Frank, Dislocation and point defects, Discussions of the Faraday Society **23**, 122–127 (1957).

[112] P. H. Dederichs and K. Schroeder, Anisotropic diffusion in stress fields, Physical Review B **17**(6), 2524 (March 1978).

[113] T. Garnier, V. R. Manga, D. R. Trinkle, M. Nastar, and P. Bellon, Stress-induced anisotropic diffusion in alloys: Complex Si solute flow near a dislocation core in Ni, Physical Review B **88**(13), 134108 (October 2013).

[114] R. L. Fleischer, Rapid solution hardening, dislocation mobility, and the flow stress of crystals, Journal of Applied Physics **33**(12), 3504–3508 (December 1962).

[115] A. H. Cottrell and B. A. Bilby, Dislocation theory of yielding and strain ageing of iron, Proceedings of the Physical Society **62**(1), 49 (1949).

[116] H. Grönbeck and V. P. Zhdanov, Effect of lattice strain on hydrogen diffusion in Pd: A density functional theory study, Physical Review B **84**(5), 052301 (August 2011).

[117] G. Kresse and J. Hafner, Ab initio molecular dynamics for liquid metals, Physical Review B **47**(1), 558 (January 1993).

[118] G. Kresse and J. Furthmüller, Efficient iterative schemes for ab initio total-energy calculations using a plane-wave basis set, Physical Review B **54**(16), 11169–11186 (October 1996).

[119] P. E. Blöchl, Projector augmented-wave method, Physical Review B **50**(24), 17953 (January 1994).

[120] G. Kresse and D. Joubert, From ultrasoft pseudopotentials to the projector augmented-wave method, Physical Review B **59**(3), 1758 (January 1999).

[121] H. M. Lawler and D. R. Trinkle, First-principles calculations of H vibrational excitations at a dislocation core of Pd, Physical Review B **82**(17), 172101 (November 2010).

[122] G. Henkelman, B. P. Uberuaga, and H. Jonsson, A climbing image nudged elastic band method for finding saddle points and minimum energy paths, Journal of Chemical Physics **113**(22), 9901–9904 (Decemeber 2000).

[123] J. Volkl and G. Alefeld, *Diffusion of hydrogen in metals*, Hydrogen in metals I, Springer Berlin Heidelberg, 1978.

[124] J. A. Yasi, L. G. Hector, and D. R. Trinkle, First-principles data for solid-solution strengthening of magnesium: From geometry and chemistry to properties, Acta Materialia **58**(17), 5704–5713 (October 2010).

[125] N. Metropolis and S. Ulam, The monte carlo method, Journal of the American statistical association **44**(247), 335–341 (1949).

[126] A. F. Voter, Introduction to the kinetic Monte Carlo method, in *Radiation effects in solids*, volume 235, Springer, 2007.

[127] U. Landman and M. F. Shlesinger, Stochastic theory of multistate diffusion in perfect and defective systems. I. Mathematical formalism, Physical Review B **19**(12), 6207 (June 1979).

[128] H. Wu, *Oxygen diffusion through Titanium and other hcp metals*, PhD thesis, University of Illinois at Urbana-Champaign, 2013.

[129] J. Voss, Q. Shi, H. S. Jacobsen, M. Zamponi, K. Lefmann, and T. Vegge, Hydrogen dynamics in Na3AlH6: a combined density functional theory and quasielastic neutron scattering study, The Journal of Physical Chemistry **111**(15), 3886–3892 (April 2007).

[130] Y. Li and G. Wahnström, Nonadiabatic effects in hydrogen diffusion in metals, Physical Review Letters **68**(23), 3444 (June 1992).

[131] Y. Li and G. Wahnström, Molecular-dynamics simulation of hydrogen diffusion in palladium, Physical Review B **46**(22), 14528 (Decemeber 1992).

[132] M. Gillan, A simulation model for hydrogen in palladium. I. Single-particle dynamics, Journal of Physics C: Solid State Physics **19**(31), 6169–6184 (1986).

[133] K. W. Kehr, D. Richter, and R. H. Swendsen, The influence of impurities on interstitial diffusion, Journal of Physics F: Metal Physics **8**(3), 433 (1978).

[134] J. W. Haus and K. W. Kehr, Diffusion in regular and disordered lattices, Physics reports **150**(5-6), 263–406 (1987).

[135] F. E. Tuddenham, H. Hedgeland, A. p. Jardine, B. A. J. Lechner, B. J. Hinch, and W. Allison, Lineshapes in quasi-elastic scattering from species hopping between non-equivalent surface sites, Surface Science **604**(17), 1459–1475 (2010).

[136] S. Paterson, C. J. Aas, and A. P. Jardine, Quasi-elastic lineshapes for atoms and simple molecules undergoing jump rotation on surfaces, Surface Science **606**(3), 426–434 (2012).

[137] C. J. Carlile and D. K. Ross, An experimental verification of the chudley-elliott model for the diffusion of hydrogen in $\alpha$-phase Pd/H, Solid State Communications **15**(11), 1923–1927 (1974).

[138] G. H. Golub and J. H. Welsch, Calculation of Gauss quadrature rules, Mathematics of Compuation **23**(106), 221–230 (1969).

[139] R. Metzler and J. Klafter, From stretched exponential to inverse power-law: Fractional dynamics, Cole-Cole relaxation processes, and beyond, Journal of Non-Crystalline Solids **305**(1), 81–87 (July 2002).

[140] L. Whitehead, R. Whitehead, B. Valeur, and M. Berberan-Santos, A simple function for the description of near-exponential decays: The stretched or compressed hyperbola, American Journal of Physics **77**(2), 173–179 (February 2009).

[141] M. Kofu, N. Hashimoto, H. Akiba, H. Kobayashi, H. Kitagawa, M. Tyagi, A. Faraone, J. R. D. Copley, W. Lohstroh, and O. Yamamuro, Hydrogen diffusion in bulk and nanocrystalline palladium: A quasielastic neutron scattering study, Physical Review B **94**(6), 064303 (August 2016).

[142] E. J. Schiavone and D. R. Trinkle, Ab inito modeling of quasielastic neutron scattering of hydrogen pipe diffusion in palladium, Physical Review B **94**(5), 054114 (August 2016).

[143] H. Jobic, M. Bee, and A. Renouprez, Quasi-elastic neutron scattering of benzene in Na-Moredenite, Surface Science **140**, 307–320 (February 1984).

[144] H. Jobic, K. Hahn, J. Kärger, M. Bee, A. Tuel, M. Noack, I. Girnus, and G. J. Kearley, Unidirectional and single-file diffusion of molecules in one-dimensional channel systems: A quasi-elastic neutron scattering study, J. Phys. Chem. B **101**(30), 5834–5841 (May 1997).

[145] K. Hahn, H. Jobic, and J. Kärger, Investigating one-dimensional diffusion by quasielastic neutron scattering: a theoretical approach., Physical Review E **59**(6), 6662–71 (June 1999).

[146] R. Ferguson, V. Arrighi, I. McEwen, S. Gagliardi, and A. Triolo, An improved algorithm for the Fourier integral of the KWW function and its application to neutron scattering and dielectric data, Journal of Macromolecular Science, Part B: Physics **45**(6), 1065–1081 (December 2006).

[147] V. Arrighi, J. Tanchawanich, and M. T. F. Telling, Molar mass dependence of polyethylene chain dynamics: A quasi-elastic neutron scattering investigation, Macromolecules **46**(1), 216–225 (Decemeber 2013).

[148] J. Pérez, J. M. Zanotti, and D. Durand, Evolution of the Internal Dynamics of Two Globular Proteins from Dry Powder to Solution, Biophysical Journal **77**(1), 454–469 (July 1999).

[149] J. Klafter and M. F. Shlesinger, On the relationship among three theories of relaxation in disordered systems, Proceedings of the National Academy of Sciences **83**(4), 848–851 (February 1986).

[150] E. Mamontov and K. W. Herwig, A time-of-flight backscattering spectrometer at the Spallation Neutron Source, BASIS, Review of Scientific Instruments **82**(8), 085109 (August 2011).

[151] G. Ehlers, A. A. Podlesnyak, J. L. Niedziela, E. B. Iverson, and P. E. Sokol, The new cold neutron chopper spectrometer at the Spallation Neutron Source: design and performance, Review of Scientific Instruments **82**(8), 085108 (August 2011).

[152] P. H. Dederichs and R. Zeller, *Point defects in metals II: Dynamical properties of point defects in metals*, Springer Tracts in Modern Physics, Springer Berlin Heidelberg, 1980.

[153] P. M. Oppeneer, A. Lodder, and R. Griessen, Resonant vibrations of hydrogen isotopes in Pd: their contributions to the electron-defect scattering, Journal of Physics F: Metal Physics **18**(8), 1743–1759 (August 1988).

[154] K. Sköld, *Hydrogen in metals I*, volume 28 of *Topics in Applied Physics*, chapter Quasielastic Neutron Scettering Studies of Metal Hydrides, Springer-Verlag Berlin Heidelberg, 1978.

[155] L. A. D. Graaf, J. J. Rush, H. E. Flotow, and J. M. Rowe, Quasielastic thermal neutron scattering by hydrogen in $\alpha$-vanadium hydride, The Journal of Chemical Physics **56**(9), 4574–4581 (May 1972).

[156] I. S. Anderson, C. J. Carlile, D. K. Ross, and D. L. T. Wilson, Intersitital interactions in the palladium-hydrogen (deuterium) system, Zeitschrift für Physikalische Chemie **115**(2), 165–175 (1979).